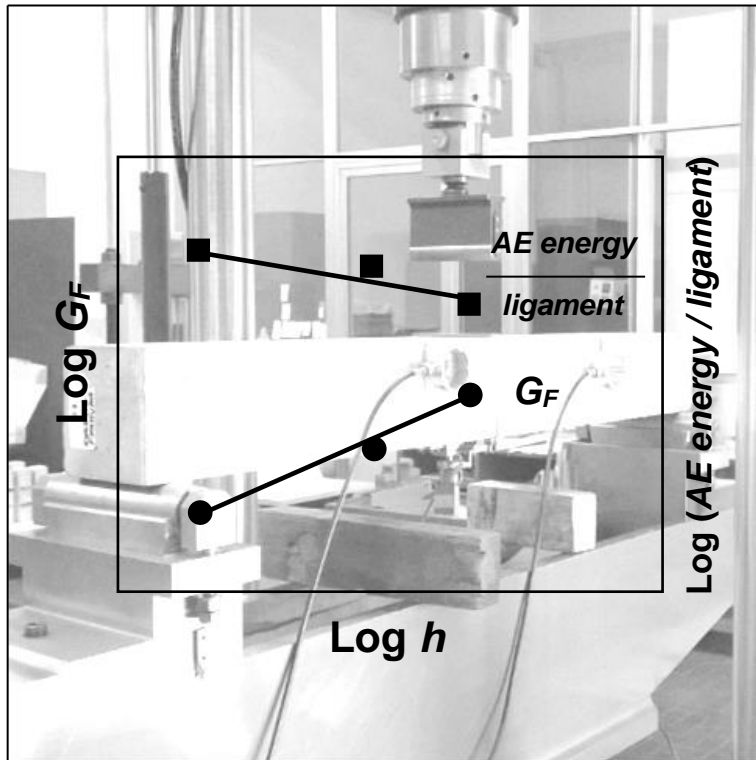


Emanuela Di Battista

# Interpretation of fracture mechanisms in ductile and brittle materials by the Acoustic Emission Technique



Dottorato di Ricerca in Ingegneria delle Strutture  
Politecnico di Torino



Emanuela Di Battista

**Interpretation of fracture mechanisms in  
ductile and brittle materials by the Acoustic  
Emission Technique**

Tesi per il conseguimento del titolo di Dottore di Ricerca  
XXVII Ciclo (2012 - 2013 - 2014)



Dottorato di Ricerca in Ingegneria delle Strutture  
Politecnico di Torino

December, 2014

PhD in Structural Engineering  
Politecnico di Torino, 24 Corso Duca degli Abruzzi, 10129 Turin, Italy

Tutor: Prof. Giuseppe Lacidogna

Coordinator: Prof. Alberto Carpinteri

# Ringraziamenti

Senza che me ne accorgessi, sono già trascorsi tre anni da quando ho iniziato il Dottorato di Ricerca.

Scrivere una tesi non è facile, in particolare quella di Dottorato richiede molto tempo, pazienza e un intenso lavoro. Ma è proprio grazie al sostegno delle persone che ti stanno vicino, al loro supporto e incoraggiamento che si riesce a raggiungere anche questo importante obiettivo.

Prima di tutto desidero fare dei doverosi ringraziamenti al mio Tutor, Prof. Giuseppe Lacidogna e al Coordinatore di Dottorato, Prof. Alberto Carpinteri. In particolare ringrazio il Prof. Lacidogna per la sua disponibilità, per avermi seguita in questi anni ed avere permesso di incrementare la mia cultura scientifica.

Un pensiero particolare va a tutta la mia famiglia, specialmente ai miei genitori e mia sorella, perché è soprattutto merito loro se sono riuscita a superare tutte le difficoltà. Mi hanno spinto a dare il meglio, a non arrendermi mai e a continuare a guardare avanti con coraggio e determinazione. Desidero ringraziare anche i piccoli Matteo, Denise e Rita che con la loro allegria e spensieratezza, mi hanno sempre fatto tornare il sorriso.

Un grazie a tutti gli altri dottorandi, in particolare ad Oscar Borla, collega di

ufficio, compagno di mille avventure, viaggi in treno e grande amico fidato. Infine, vorrei ringraziare anche tutti i miei amici che mi sono stati sempre vicini, credendo in me, aiutandomi nei momenti difficili e facendomi divertire.

Senza tutte queste persone non sarei riuscita a raggiungere questo importante traguardo.

Grazie a tutti.

## **Summary**

Nowadays, the measure of the damage phenomena inside a structure is a complex problem that requires the use of innovative Structural Health Monitoring (SHM) and non-destructive investigation methodologies. The non-destructive method based on the Acoustic Emission (AE) technique has proved highly effective, especially to predict fracture behavior that take place inside a material subjected to mechanical loading.

Objective of the research is to use the Acoustic Emission monitoring to evaluate the fracture propagation process during tensile tests, three-point bending (TPB) tests and compression tests. The most representative AE parameters have been measured by sensors in order to obtain detailed information on the wave propagation velocity, signals localization as well as on the dominant fracture mode. As a matter of fact, the waves frequency and the Rise Angle are used to discriminate the prevailing cracking mode from pure opening or sliding. Moreover, the cumulated number of AE events and their amplitude are used to compute the signal energy. For the three-point bending tests on concrete beams, the energy dissipated to create the fracture surfaces and the energy emitted and detected by the AE sensors have been compared on the basis of their cumulative

value at the end of the test and their rate during the process loading, in order to investigate on their correlation.

A numerical simulation of the mechanical response of the TPB tests has been also performed on the basis of the cohesive crack model. This approach has permitted to obtain a step-by-step evaluation of the crack propagation and a more detailed analysis of the mechanical energy dissipation rate during the loading test.

In addition, a dedicated in-situ monitoring at the San Pietro - PratoNuovo gypsum quarry located in Murisengo (AL) - Italy, is started and it is still in progress, developing the application aspects of the AE technique, which has been widely studied from a theoretical and experimental point of view by some Authors in the safeguard of civil and historical buildings.

Preliminary laboratory compression tests on gypsum specimens with different slenderness ( $\lambda=0.5$ ,  $\lambda=1$ ,  $\lambda=2$ ) were conducted to assess the validity and efficiency of the system in view to a permanent installation for *in-situ* monitoring.

Currently the quarry is subjected to a multiparameter monitoring, by the AE technique and the detection of the environmental neutron field fluctuations, in order to assess the structural stability and, at the same time, to evaluate the seismic risk of the surrounding area.

# Sommario

Al giorno d'oggi la valutazione del danneggiamento all'interno di una struttura è un problema complesso, che richiede l'utilizzo di un monitoraggio strutturale innovativo (Structural Health Monitoring, SHM) e metodologie di indagine non distruttive. Il metodo non distruttivo basato sulla Tecnica delle Emissioni Acustiche (TEA) si è dimostrato particolarmente efficace, soprattutto nel prevedere il comportamento a frattura di un materiale sottoposto a carico meccanico.

L'obiettivo di questa tesi di ricerca è quello di valutare il processo di propagazione della frattura durante prove di trazione, prove di flessione su tre punti (Three Point Bending, TPB) e prove di compressione, utilizzando il monitoraggio delle Emissioni Acustiche. I principali parametri di Emissione Acustica sono stati misurati tramite sensori piezoelettrici al fine di ottenere informazioni dettagliate circa la velocità di propagazione delle onde, la localizzazione dei segnali, ma anche il modo di frattura dominante. La frequenza delle onde e il Rise Angle, infatti, permettono di determinare il modo prevalente di fessurazione: pura apertura o scorrimento. Inoltre, il numero cumulato di eventi di Emissione Acustica e la loro ampiezza sono stati utilizzati per calcolare l'energia

del segnale acustico.

Per le prove di flessione su tre punti su travi in calcestruzzo, l'energia dissipata per creare le superfici di frattura è stata confrontata con l'energia emessa (ossia quella rilevata dai sensori piezoelettrici) sulla base del loro valore cumulativo alla fine del test e il loro rate durante il processo di carico, in modo da poter indagare la loro correlazione.

E' stata inoltre eseguita una simulazione numerica basata sul modello della fessura coesiva per valutare la risposta meccanica delle prove TPB. Questo approccio ha permesso di determinare passo dopo passo sia la propagazione della fessura, ma anche di ottenere un'analisi più dettagliata del rate di dissipazione dell'energia meccanica durante la prova di carico.

Considerando, inoltre, che la tecnica delle Emissioni Acustiche è già stata ampiamente studiata da alcuni Autori da un punto di vista teorico e sperimentale nell'ambito della salvaguardia di edifici civili e storici, è stato avviato ed è tuttora in corso, un monitoraggio *in-situ* presso la cava di gesso San Pietro - Prato Nuovo situata a Murisengo (AL) - Italia, con il fine di sviluppare gli aspetti applicativi di questa tecnica anche in ambito geotecnico.

Sono state eseguite prove sperimentali preliminari di compressione su provini di gesso di snellezza differente ( $\lambda=0.5$ ,  $\lambda=1$ ,  $\lambda=2$ ) per valutare la validità e l'efficienza del sistema in vista di una installazione permanente per il monitoraggio *in-situ*.

Attualmente la cava è sottoposta ad un monitoraggio multiparametrico tramite la tecnica di EA e la rilevazione delle fluttuazioni ambientali di neutroni, al fine di valutarne la stabilità strutturale e, allo stesso tempo, valutare il rischio sismico a cui è soggetta l'area circostante.

# Contents

▪ Ringraziamenti.....	III
▪ Summary.....	V
▪ Sommario.....	VII
<b>1 Acoustic Emission Technique.....</b>	<b>1</b>
1.1 Structural Health Monitoring (SHM) and Non-destructive Tests (NDT) 1	
1.2 Acoustic Emission Testing (AET).....	6
1.2.1 Acoustic Emission Waves and Signal Waves .....	6
1.2.2 Measuring System .....	9
1.2.3 Event Counting and Ring-Down Counting .....	10
1.2.4 AE Source Location .....	11
1.3 Fractal dimension of the damage domain.....	20
1.3.1 Energy Density Criterion.....	20
1.3.2 Statistical Distribution of AE Events: the <i>b</i> -Value analysis.....	22
1.3.3 Regional Seismicity and AE Structural Monitoring.....	25
<b>2 Ductile and Brittle Materials: Damage and Failure Characterization....</b>	<b>27</b>
2.1 Introduction: Ductile and Brittle Materials .....	27
2.2 Damage and Failure Characterization of Structural Materials .....	29
2.3 Theoretical Models.....	31
2.3.1 Uniaxial Tensile .....	31
2.3.2 Uniaxial compression.....	34
2.3.3 Three point bending.....	39

2.3.3.1	The Cohesive Crack Model .....	41
---------	--------------------------------	----

### **3 Laboratory Tests and Energies Analysis with the AE Monitoring in Brittle and Quasi-brittle Materials..... 47**

3.1	Introduction: the Acoustic Emission Technique.....	47
3.2	Experimental tests.....	53
3.2.1	Uniaxial tensile tests .....	53
3.2.1.1	AE source localization .....	57
3.2.1.2	Wave propagation velocity, frequencies and wavelength.....	60
3.2.1.3	Identification of the fracture mode .....	63
3.2.2	Three point bending tests (TPB).....	65
3.2.2.1	AE parameters analysis.....	68
3.2.2.2	Dissipated vs. emitted energy.....	76
3.2.2.3	Dissipated and emitted energy rates.....	82
3.2.3	Uniaxial compression tests .....	89
3.3	Conclusions .....	93
3.3.1	Uniaxial tensile tests.....	93
3.3.2	Three Point Bending tests.....	94
3.3.3	Uniaxial compression tests .....	96

### **4 Case Study: In-situ Monitoring at the San Pietro-Prato Nuovo Gypsum Quarry located in Murisengo (Alessandria), Italy..... 97**

4.1	Introduction: The San Pietro-Prato Nuovo Gypsum Quarry .....	97
4.2	The structural monitoring .....	98
4.2.1	AET and NET Monitoring Setup.....	99
4.2.2	Experimental tests.....	100
4.2.3	In-situ monitoring .....	103
4.2.3.1	AE source localization .....	107

---

4.3	Damage evaluation of the monitored pillar by AE.....	109
4.3.1	A fractal criterion for AE monitoring.....	109
4.3.2	Critical behavior interpreted by AE .....	111
4.3.3	Damage level of the monitored pillar .....	113
4.4	Conclusions .....	115
4.4.1	Experimental compression tests .....	115
4.4.2	In-situ monitoring.....	115
4.4.3	Damage evaluation by AE.....	116
<b>5</b>	<b>Conclusions .....</b>	<b>119</b>
5.1	Experimental tests.....	119
5.2	In-situ Monitoring at the Gypsum Quarry (Murisengo, Italy).....	121
<b>6</b>	<b>References.....</b>	<b>123</b>



# **1 Acoustic Emission Technique**

## **1.1 Structural Health Monitoring (SHM) and Non-destructive Tests (NDT)**

Structural Health Monitoring (SHM) allows to provide accurate and in-time information concerning the physical conditions and performance of in-service structures. Its purpose is to detect the structural behavior in quasi-real-time, indicate the approximate position of problems on the structure and the importance of them.

The information obtained from monitoring is generally used to plan and design maintenance activities, increase the safety and reduce uncertainty in civil structures, in order to assure an extension of their service life.

From a general point of view, "damage" is defined as changes to the material and/or geometric properties of structural systems, including changes to the boundary conditions and system connectivity, which adversely affect the system's performance.

A wide variety of highly effective Structural Health Monitoring tests are available. The tests named as Non Destructive Tests (NDT), or Non Destructive Evaluation (NDE) and Non Destructive Inspection (NDI), are a group of methods

in which the damaging of materials and the pulling out of specimens from the considered structure are not necessary. Whereas NDE aims to measure mechanical and/or structural materials properties; NDT aims to search for and characterize the defects which can diminish the mechanical qualities, and even to lead to the failure of the material or structure. However, these two fields are deeply linked, as each measurement of property can be used for testing (Bruneau and Potel, 2009).

These methods are based on X-ray, electromagnetic induction, penetrating liquids, thermographs, endoscopies, extensometers, optical interferometers, ultrasonic radiation and acoustic emission.

Techniques based on generation and propagation of mechanical waves, so-called acoustic waves, constitute an important part of the NDT applied to building materials.

An advanced method of quantitative non-destructive evaluation of damage progression is represented by the Acoustic Emission (AE) Technique. Technically, the expression "acoustic emission" (AE) is used for a class of phenomena in which transient elastic waves are generated by the rapid release of energy from localized sources, typically developing cracks within a material (Ohtsu 1996; Carpinteri and Lacidogna, 2003; Carpinteri et al., 2006 a,b,c,d). Other terms used in AE literature include "stress wave emission" and "microseismic activity". Acoustic emission occurs in a range of intensities with different phenomena. The sound of a broken pencil lead is a typical example of AE on a small scale. An earthquake is an example of AE on a large scale. The AE generation mechanism is the same: it is due to a release of elastic energy into AE waves by the formation of a crack in a solid (Katsuyama, 1994).

In contrast to other non-destructive testing methods, as the ultrasound method, AE technique is the only one that allows the monitoring of progression damage, because the signals are produced by a growing damage. It does not require external energy, as a matter of fact acoustic emission is released from the tested object itself. Furthermore, AE is the only NDT method that can be used to monitor defects during manufacturing. Other conventional NDT methods require the line to be interrupted (Kawamoto and Williams, 2002).

AE technique, originally used to detect cracks and plastic deformations in metals, has been applied to studies and research in the field of rocks and then extended to a wide range of materials. The use of AE technique has recently spread to the investigation of concrete materials as well. Concrete differs from the above mentioned materials by its heterogeneity, its high attenuation, and the large dimensions of the structures (Ohtsu, 1996).

The field of application starts with laboratory tests and ends up with in-situ testing of full-scale structures. Some laboratory models can also be used to quantify a safety indicator and to compare it to required levels in order to determine the remaining life potential of the structure. It should be noted that, during the measurement, the huge variability of some non-controlled parameters of the material, or of environmental conditions, imposes the need for caution when considering the absolute threshold.

However, Acoustic Emission Testing (AET), represents a competitive tool of structural health testing and monitoring of structures and materials, namely having been in service for many years. In parallel, recent progress in AET shows that this method allows us to follow in real time, while a part is being stressed, the damage, and to characterize quantitatively and qualitatively these mechanisms (Bruneau and Potel, 2009).

In general, sources of AE are due to cracking, friction, impact, phase changes, magnetic processes, etc.

Loading produces a stress field which is further amplified closer to preexisting defects causing the AE (Pollock, 1968). More precisely, a microcrack is nucleated by the rupture of a bond at a weak spot where stress concentrates (Figure 1.1a). The stress on the failed bond is suddenly redistributed through propagating elastic waves, which are called AE waves (Figure 1.1b). The transient stress wave ends when a new equilibrium configuration, in which the resulting forces acting on each volume element vanish, is reached (Figure 1.1c).

AE waves propagate through the material towards the surface of the structural element, where they can be detected by sensors which turn the released strain energy packages into electrical signals. Figure 1.2 illustrates this principle.

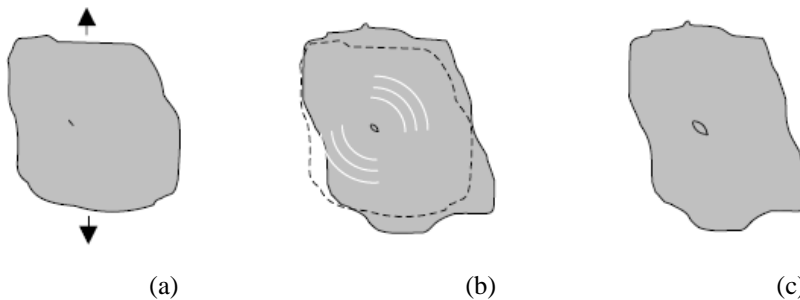


Figure 1.1: (a) Acoustic emission generated by the formation of a microcrack: (a) initiating microcrack in a weak spot; (b) opening of microcrack; (c) arrest of microcrack.

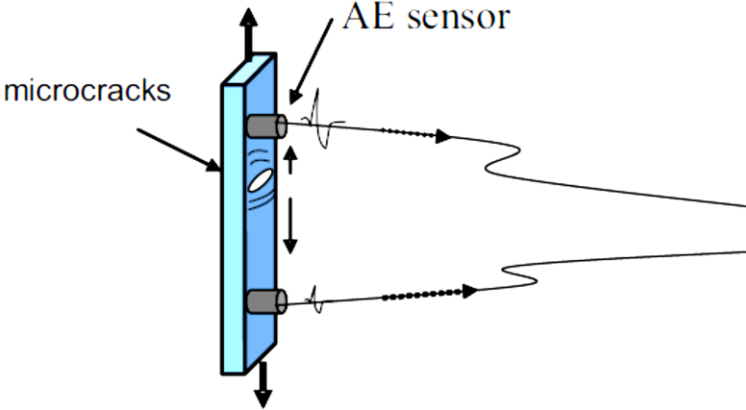


Figure 1.2: Principle of AET: stressed material generating an elastic wave.

## 1.2 Acoustic Emission Testing (AET)

### 1.2.1 Acoustic Emission Waves and Signal Waves

The Acoustic Emission (AE), which corresponds to the elastic energy radiated by the stressed material, has many advantages, in particular this technique is a passive testing applicable on structures in use.

An AE wave is characterized by a wide frequency range (from kHz to MHz) and the maximum duration of the emitted wave is equal to the time during which the defect is in motion (Brindley et al., 1973). For crack velocities approaching the speed of sound, this implies durations of  $\sim 10^{-8}$ s for crack propagation through  $\sim 100$   $\mu\text{m}$  in concrete. Physically, AE waves consist of P-waves or longitudinal waves, S-waves or shear waves, and surface waves or Rayleigh waves (Figure 1.3).

An AE signal wave is the electrical output signal recorded by the AE equipment. The output signals are the combination of AE waves, effects related to the propagation in the material and the sensor response. Generally speaking, after few oscillations the signal is more dominated by side reflections or other influences related to the heterogeneity of material or the sensor characteristics (sensor resonance, etc.) than by the source (Ohtsu, 1996).

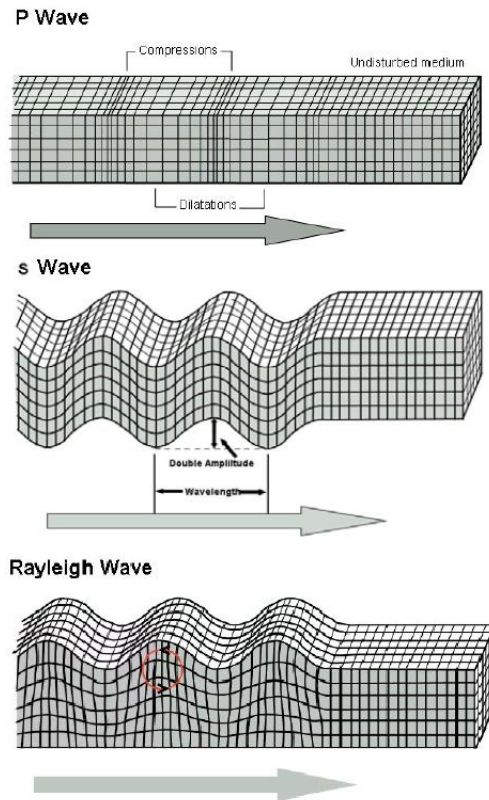


Figure 1.3: Wave propagation modes in an elastic medium.

Most of the AE data analyses are based on a conventional evaluation of some parameters such as signal amplitude, duration, energy, count number etc.

Figure 1.4 represents a typical AE signal. On these signals, several parameters can be defined as indicated by RILEM (RILEM, 1986; RILEM, 2010a; RILEM, 2010b; RILEM, 2010c).

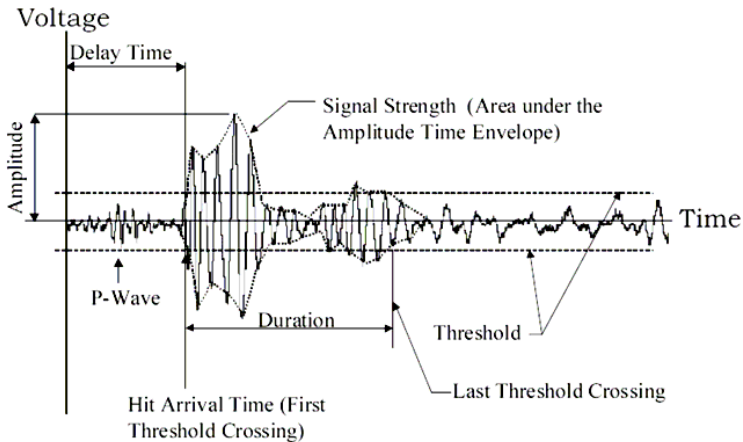


Figure 1.4: AE signal and its main parameters.

*Amplitude:* the peak voltage of the largest amplitude value in a waveform. Its unit of measure is Decibel (dB). The amplitude expressed in dB is related to that one measured in Volt ( $A_{MAX}$ ) by the equation (Tinkey et al., 2002; Colombo et al., 2003; Rao and Lakshmi, 2005):

$$A_{dB} = 20 \text{Log}_{10} \left( \frac{V}{V_0} \right) \quad (1.1)$$

*Duration:* the time observed from the first arrival to the time when the amplitude decays up to the level lower than the threshold.

*Voltage threshold:* a voltage level on an electronic comparator. Only those signals with absolute amplitude larger than this level will be recognized.

### 1.2.2 Measuring System

Acoustic Emission sensors can be divided into two categories: resonant and wideband. The first type is more sensitive at certain frequencies, which depend on the internal resonant frequency of a piezoelectric (PZT) crystal.

Resonant sensors exploit the capacity of these PZT crystals to produce electric signals whenever they are subjected to a mechanical stress. A typical AE sensor changes elastic vibrations, i.e. stress waves, into electric signals.

Wideband sensors, instead, use an energy-absorbing backing material to damp out the predominant frequencies. This allows to cover a wider frequency range but lower sensitivity. Sensors with bandwidth extending to  $\sim 100$  MHz would be necessary to fully reproduce the waveform.

The choice of the most appropriate AE transducer depends on the purpose of the measurement. For a material characterized by high attenuation, low resonant AE transducers should be used, while for the waveform analysis, flat non-resonant ones are better. Both kind of sensors filter out low frequency disturbances signals (below 50 kHz) coming from the environmental noise.

In the presented case studies, two kinds of sensors were used. During the experimental tests, each specimen was monitored by the AE technique. The AE signals have been detected by piezoelectric (PZT) transducers, attached on the surface of the specimens. The sensors, sensitive in the frequency range from 80 to 400 kHz for high-frequency AEs detection, are produced by LEANE NET s.r.l. (Italy). The connection between the sensors and the acquisition device is realized by coaxial cables in order to reduce the effects of electromagnetic noise.

As regarding the gypsum quarry monitoring, six USAM® sensors which cover signals in the range between 100 and 500 kHz, have been used.

### 1.2.3 Event Counting and Ring-Down Counting

AE wave can be detected in the form of hits on one or more channels. A "hit" is the term to indicate that a given AE channel has detected and processed one AE transient signal. One "event" is a group of AE hits received from a single source by two or more channels, of which spatial coordinates could be located.

During a monitoring process the occurrences of AE events are counted. Event counting is carried out by setting the dead time or rectifying the signal waveform into an envelop (Figure 1.5). Therefore, the number of event counts should correspond closely to the occurred AE events (Kawamoto and Williams, 2002).

The principle of ring-down counting, instead, is to count the number of times  $n_0$  a threshold voltage  $A_{th}$  is exceeded by the burst of oscillations caused by each single AE event (Pollock, 1973; Brindley et al., 1973). Major requirement to carry out this particular counting technique is a dead time as short as possible.

The difference between event and ring-down counting methods is clear in Figure 1.5.

One advantage obtained in ring-down counting is that the count related from a given event increases with signal amplitude and there is consequently some weighting in favour of events of larger energy (Brindley et al., 1973).

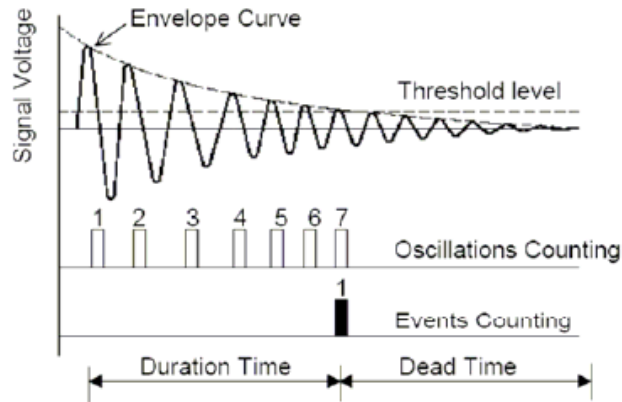


Figure 1.5: Counting methods for AE events: oscillation (ring-down) counting and event counting from an AE waveform.

#### 1.2.4 AE Source Location

Acoustic Emissions fall within the class of phenomena in which transient elastic waves are generated by the rapid release of elastic energy by localized sources in material bulk. All building and construction materials produce AE during cracks generation and propagation. Elastic waves propagate through the solid to the surface, where they are detected by AE sensors. Processing these signals, it is possible to get information on the existence and location of AE sources, i.e. where the solid is damaging.

In the most cases, during AE data analysis, the wave propagation speed  $v$  is hypothesized constant in the material and its value is an input data for the resolution of the AE source location problem. So, from the point of view of the elastic waves propagation, the solid is considered as a homogeneous and isotropic

medium, in which the wave fronts propagate along straight rays, in a similar way to what happens in geometrical optics. It is possible to apply the laws of kinematics of uniform rectilinear motion to describe the propagation of these rays (Lagrange, 1788). The assumptions of point source and the homogeneity (rectilinear propagation) and isotropy (the velocity of propagation is the same in all directions) of the analyzed material, make it possible to consider the wavefronts as spherical surfaces.

When a solid has a dominant dimension with respect to the other two, the problem can be reduced as one-dimensional: we consider that the sensors and the source are on the same axis that corresponds to the solid axis. It is assumed that the source  $S$  is located between the two sensors  $S_1$  and  $S_2$  as shown in Figure 1.6.



Figure 1.6: AE source localization - One-dimensional solid, with  $x_1 < x < x_2$ .

From kinematics, we have:

$$\begin{cases} x - x_1 = v(t_1 - t_0) \\ x_2 - x = v(t_2 - t_0) \end{cases} \quad (1.2)$$

in which  $v$  is the wave speed. Therefore:

$$x = \frac{1}{2}(x_2 + x_1) - \frac{1}{2}v(t_2 - t_1) \quad (1.3)$$

It is observed, from the latter equation, that the AE source  $S$  locating problem is completely solved if the instants of detection of the AE signal by the two sensors, and their positions are known. Consider now the situation in which the source  $S$  is located outside of the portion of the solid between the two sensors. Let consider the case  $x_1 < x_2 < x$  summarized in Figure 1.7.

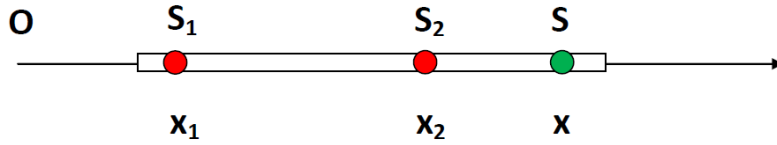


Figure 1.7: AE source localization: One-dimensional solid, with  $x_1 < x_2 < x$ .

From kinematics, we have:

$$\begin{cases} x - x_2 = v(t_2 - t_0) \\ x - x_1 = v(t_1 - t_0) \end{cases} \quad (1.4)$$

and, therefore:

$$2x = v(t_1 + t_2 - 2t_0) + (x_1 + x_2). \quad (1.5)$$

From the latter equation it can be seen that, unless the instant  $t_0$  of the signal emission is known, the location of the AE source  $S$  is a problem that admits infinite solutions, compatible with the data of the problem. In other words, it expresses the obvious fact that  $x$  is defined up to an arbitrary additive constant: in fact, if  $S$  moves along the axis, the paths that the ray makes to get to the two sensors differ always of the same quantity, for which the relative delay between the instants of detection remains unchanged. Therefore, it is possible to conclude that in the one-dimensional case, to locate  $S$  is necessary to position the sensors at the ends of the beam, otherwise the solution is indefinite.

To determine the AE sources in a thin flat plate, the problem can be represented in two dimensions: the sensors and the source  $S$  are lying on the same plane, where the propagation of elastic waves takes place on.

Generally speaking, it is not possible to locate  $S$  in the plane if only the instants of detection of two sensors are known. In fact, if plane polar coordinates  $(r, \theta)$  are used, we have:

$$\begin{cases} r_1 = v(t_1 - t_0) \\ r_2 = v(t_2 - t_0) \end{cases} \quad (1.6)$$

and, therefore:

$$r_2 - r_1 = v(t_2 - t_1) = v\Delta t_{21}. \quad (1.7)$$

The experimental data provide  $\Delta t_{21}$  for which it is possible to obtain only the difference  $r_2 - r_1$  of the paths which "hit" the sensors  $S_1$  and  $S_2$  from  $S$ . The experimental data can be associated to AE occurred in another place and at a different instant, because:

$$r'_2 - r'_1 = v(t_2 - t'_0) - v(t_1 - t'_0) = v\Delta t_{21} \quad (1.8)$$

and, therefore:

$$r'_2 - r'_1 = r_2 - r_1 = cost. \quad (1.9)$$

Considering that hyperbola is the locus of points on the plane for which is constant the difference of the distances from two fixed points  $F_1$  and  $F_2$ , called foci, it follows that the geometric locus on which the source may be compatible with  $t_2$  and  $t_1$  is a hyperbola branch that has to ring the points in which sensors  $S_1$  and  $S_2$  are positioned.

In a plane, the coordinates that identify a point are two, for which you have to set up a system for solving two equations in two unknowns that identify  $S$ . So, it is necessary to have two information in terms of time, i.e. the relative delays between the two sensors with respect to a third, taken as reference. The problem, outlined in the following figure, is set in the plane polar coordinates  $(r, \theta)$ :

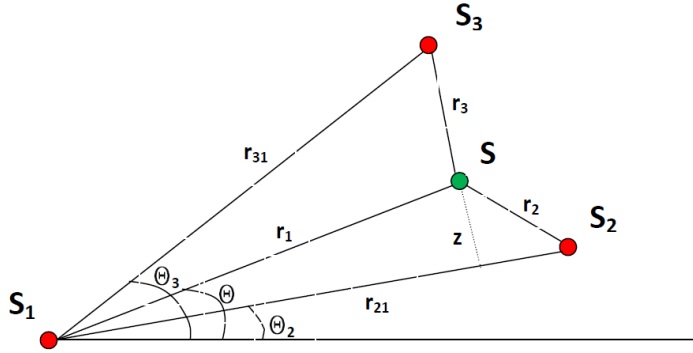


Figure 1.8: AE source and sensors: Polar coordinates system.

From Figure 1.8, considering the triangle  $S, S_1, S_2$ , we have:

$$r_2 - r_1 = v\Delta t_{21}, \quad (1.10)$$

$$z = r_1 \sin(\theta - \theta_2), \quad (1.11)$$

$$z^2 = r_2^2 - [r_{21} - r_1 \cos(\theta - \theta_2)]^2. \quad (1.12)$$

Substituting Eq.(1.11) in Eq.(1.12), we have:

$$r_1^2 = r_2^2 - r_{21}^2 + 2r_{21}r_1 \cos(\theta - \theta_2). \quad (1.13)$$

Eliminating  $r_2$  and taking into account  $r_1 = v(t_1 - t_0)$ :

$$r_1 = \frac{r_{21}^2 - \Delta t_{21}^2 v^2}{2(\Delta t_{21} v + r_{21} \cos(\theta - \theta_2))}. \quad (1.14)$$

In a similar way, considering the triangle  $S, S_1, S_3$  and taking into account that:

$$r_3 - r_1 = (t_3 - t_1)v = \Delta t_{31} v, \quad (1.15)$$

we have:

$$r_1 = \frac{r_{31}^2 - \Delta t_{31}^2 v^2}{2(\Delta t_{31} v + r_{31} \cos(\theta_3 - \theta))}. \quad (1.16)$$

Eqs.(1.14) and (1.16) allow to localize  $S$ . From the geometric point of view the solution represents the intersection between two branches of two hyperbolas: the first having foci in  $S_1$  and  $S_2$ ; while the second in  $S_1$  and  $S_3$ . The solution is not necessarily unique: that is deducible from the non-linearity of Eqs.(1.14) and (1.16) in  $r_1$  and  $\theta$ . The problem of double intersections should be addressed on a case by case basis: the problem goes away when one of the two solutions is physically unacceptable, so when it detects a point external to the plane.

If we have AE data from four sensors belonging to a plane, we have the opportunity to write three linearly independent equations with the delays of three sensors compared to the fourth. It sets three linear equations in three unknowns of which two are spatial and one is temporal. Assuming that an AE in  $S$  at time  $t_0$  is picked up by the four sensors, the following equations are deduced ( $\Delta t_i = t_i - t_0$ ):

$$\begin{aligned}
v^2(\Delta t_1)^2 &= (x - x_1)^2 + (y - y_1)^2 \\
v^2(\Delta t_2)^2 &= (x - x_2)^2 + (y - y_2)^2 \\
v^2(\Delta t_3)^2 &= (x - x_3)^2 + (y - y_3)^2 \\
v^2(\Delta t_4)^2 &= (x - x_4)^2 + (y - y_4)^2
\end{aligned} \tag{1.17}$$

from which, by developing the square and subtracting the first equation from the other, we obtain (1.18):

$$\begin{aligned}
2(x_2 - x_1)x + 2(y_2 - y_1)y + 2v^2(t_2 - t_1)\Delta t_1 &= (x_2^2 + y_2^2) - \\
&(x_1^2 + y_1^2) - v^2(t_2 - t_1)^2 \\
2(x_3 - x_1)x + 2(y_3 - y_1)y + 2v^2(t_3 - t_1)\Delta t_1 &= (x_3^2 + y_3^2) - \\
&(x_1^2 + y_1^2) - v^2(t_3 - t_1)^2 \\
2(x_4 - x_1)x + 2(y_4 - y_1)y + 2v^2(t_4 - t_1)\Delta t_1 &= (x_4^2 + y_4^2) - \\
&(x_1^2 + y_1^2) - v^2(t_4 - t_1)^2
\end{aligned}$$

Eqs.(1.18) constitute a linear system in the unknowns  $x$ ,  $y$ ,  $\Delta t_1$  that determines the position  $(x, y)$  and the instant of emission  $t_0$  of the source  $S$ . Therefore, due to the linearity of the equations, the position  $(x, y)$  is uniquely determined. The critical case is that in which the rank of the coefficient matrix is  $< 3$ : in this case the system admits infinite solutions, i.e. the system is indeterminate. Typically critical cases are those in which three or four sensors are aligned.

The initial assumptions of homogeneity and isotropy of the material are subjected to some criticism. As a matter of fact, the homogeneous and isotropic solid model is an approximation of reality, and the way the waves actually propagate in the material is more similar to that shown in Figure 1.9.

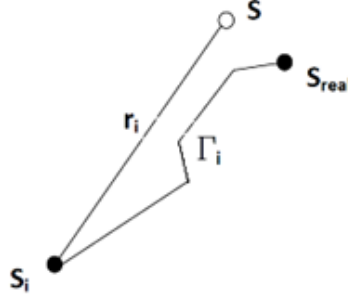


Figure 1.9: AE wave propagation path model.

This concept is summarized by Eq.(1.19), where  $\Gamma_i$  is the actual path of the signal from the real source  $S_{real}$  to the sensor  $S_i$ ,  $u_i$  it is the local unit vector tangent to  $\Gamma_i$  and  $r_i$  is the modulus of the radius vector from the estimated source  $S$  to  $S_i$ :

$$\int_{\Gamma_i} \vec{u}_T \cdot d\vec{r} \equiv \int_{\Gamma_i} ds \neq r_i \quad (1.19)$$

The relationship between the adopted model of homogeneous and isotropic solid and the real solid is the following:

$$\Delta t_i = t_i - t_0 = \int_{\Gamma_i} \frac{ds}{v(r)} + m_i = \frac{r_i}{v} \quad (1.20)$$

where  $m_i$  is the error that affects the experimental data and  $v$  is the propagation speed chosen as constant for the model. Eq.(1.20) has only formal value because both  $\Gamma_i$  and  $v(r)$ , that define exactly the propagation of waves in the solid, remain unknown. Eq.(1.19) still shows that we are unable to determine the exact position of the source: only an approximation is possible.

Moreover, the wave propagation speed is considered as a constant and it is fixed at the beginning of each AE data analysis. So a not-real estimation of this speed can lead to considerable errors in the AE source localization. Furthermore, even if we have correctly estimated an average value of wave speed, the described approach could not take into account any local gradients of propagation velocity.

### 1.3 Fractal dimension of the damage domain

Two different approaches are proposed to obtain indirect estimation of the physical fractal dimension of the damage domain up to the peak load of quasi-brittle materials, such as concrete and rocks. First, an energy density approach is presented, based on the size-effects of the energy release determined by the AE technique. The second one is a complementary method, based on the  $b$ -value analysis of AE events (Scholz, 1968). Since the  $b$ -value is size-independent, its evaluation evidences the similarity between the damage process in a structure and the seismic activity in a region of the Earth crust (Scholz, 1968).

#### 1.3.1 Energy Density Criterion

Acoustic Emission data have been interpreted by means of statistical and fractal analysis, considering the multiscale aspect of cracking phenomena (Carpinteri et al., 2007a). Consequently, a multiscale criterion to predict the damage evolution has been formulated. Recent developments in fragmentation theories (Carpinteri et al., 2002) have shown that during microcrack propagation, the energy  $W$  is dissipated over a fractal domain comprised between a surface and the specimen volume  $V$ .

The following size-scaling law has been assumed during the damage process:

$$W \propto N \propto V^{D/3} . \tag{1.21}$$

where  $D$  is the so-called fractal exponent comprised between 2 and 3, and  $N$  is the cumulative number of AE events that the structure provides during the damage monitoring.

Some Authors have also shown that energy dissipation, as measured with the AE technique during the damaging process, follows the time-scaling law (Carpinteri et al., 2005):

$$W \propto N \propto t^{\beta_t}, \quad (1.22)$$

where  $\beta_t$  is the time-scaling exponent for the dissipated energy in the range (0, 3) and  $N$  is the number of AE events.

By working out the exponent  $\beta_t$  from the data obtained during the observation period, we can make a prediction on the structure's stability conditions (Carpinteri et al., 2005; Carpinteri et al., 2007), as shown in Figure 1.10:

- if  $\beta_t < 1$ , the damaging process slows down, because energy dissipation tends to decrease;
- if  $\beta_t > 1$  the process becomes unstable,
- if  $\beta_t \approx 1$  the process is metastable, it can reach either stability or instability conditions indifferently.

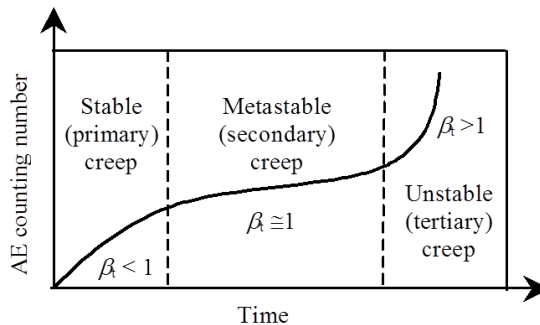


Figure 1.10: Structure's stability conditions as a function of the  $\beta_t$  coefficient.

### 1.3.2 Statistical Distribution of AE Events: the $b$ -Value analysis

A statistical interpretation of the variation in the  $b$ -value during the damage evolution detected by AE has been presented, which is based on a treatment originally proposed by Carpinteri and co-workers (Carpinteri, 1994; Carpinteri et al., 2008a). This model captures the transition from the condition of diffused criticality to that of imminent failure localization.

By analogy with seismic phenomena, in the AE technique the magnitude may be defined as follows:

$$m = \text{Log}_{10} A_{max} + f(r) \quad (1.23)$$

where  $A_{max}$  is the amplitude of the signal expressed in Volt, and  $f(r)$  is a correction factor taking into account that the amplitude is a decreasing function of the distance  $r$  between the source and the sensor.

In seismology the empirical Gutenberg-Richter's law (Richter, 1958):

$$\text{Log}_{10} N(\geq m) = a - bm, \text{ or } N(\geq m) = 10^{a-bm}, \quad (1.24)$$

expresses the relationship between magnitude and total number of earthquakes with the same or higher magnitude in any given region and time period, and it is the most widely used statistical relation to describe the scaling properties of seismicity. In Eq. (1.24),  $N$  is the cumulative number of earthquakes with magnitude  $\geq m$  in a given area and within a specific time range, while  $a$  and  $b$  are positive constants varying from a region to another and from a time interval to another. Equation (1.24) has been used successfully in the AE field to study the scaling laws of AE wave amplitude distribution. This approach evidences the

similarity between structural damage phenomena and seismic activities in a given region of the Earth's crust, extending the applicability of the Gutenberg-Richter's law to Structural Engineering. According to Eq. (1.24), the  $b$ -value changes systematically at different times during the damage process and therefore it can be used to estimate damage evolution modalities.

Equation (1.24) can be rewritten in order to draw a connection between the magnitude  $m$  and the size  $L$  of the defect associated with a AE event. By analogy with seismic phenomena, the AE crack size-scaling entails the validity of the relationship:

$$N(\geq L) = cL^{-2b}, \quad (1.25)$$

where  $N$  is the cumulative number of AE events generated by source defects with a characteristic linear dimension  $\geq L$ ,  $c$  is a constant of proportionality, and  $2b = D$  is the fractal dimension of the damage domain.

It has been evidenced that this interpretation is based on the assumption of a dislocation model for the seismic source and requires that  $2.0 \leq D \leq 3.0$ , i.e., the cracks are distributed in a fractal domain comprised between a surface and the volume of the analyzed region (Turcotte, 1997; Rundle et al., 2003).

The cumulative distribution (Eq.1.25) is substantially identical to that proposed by Carpinteri (Carpinteri, 1994), which gives the probability of a defect with size  $\geq L$  being present in a element:

$$P(\geq L) \propto L^{-\gamma}. \quad (1.26)$$

Therefore, the number of defects with size  $\geq L$  is:

$$N^*(\geq L) = cL^{-\gamma} \quad (1.27)$$

where  $\gamma$  is a statistical exponent measuring the degree of disorder, i.e. the scatter in the defect size distribution, and  $c$  is a constant of proportionality. By equating distributions (1.25) and (1.27) it has been found that:  $2b = \gamma$ . When the collapse is reached, the size of the maximum defect is proportional to the characteristic size of the structure. As shown by Carpinteri and co-workers (Carpinteri et al., 2008a), the related cumulative defect size distribution (referred to as self-similarity distribution) is characterized by the exponent  $\gamma = 2.0$ , which corresponds to the minimum value  $b = 1.0$ . It was also demonstrated by Carpinteri (Carpinteri et al., 2008a) that  $\gamma = 2.0$  is a lower bound observed experimentally when the load bearing capacity of a structural member has been exhausted.

Therefore, by determining the  $b$ -value it is possible to identify the energy release modalities in a structural element during the monitoring process. The extreme cases envisaged by Eq. (1.21) are  $D = 3.0$ , which corresponds to the critical condition  $b = 1.5$ , when the energy release takes place through small defects homogeneously distributed throughout the volume, and  $D = 2.0$ , which corresponds to  $b = 1.0$ , when energy release takes place on a fracture surface. In the former case diffused damage is observed, whereas in the latter two-dimensional cracks are formed leading to the separation of the structural element.

### 1.3.3 Regional Seismicity and AE Structural Monitoring

Among the various studies on the earthquakes space-time correlation, there is a statistical method that allows to calculate the degree of correlation both in space and time between a series of AE and the local seismic recordings, collected in the same period. This analysis is based on the generalization of the space-time correlation known as the integral of Grassberger-Procaccia (Grassberger and Procaccia, 1983), defined as follows:

$$C(r, \tau) \equiv \frac{1}{N_{EQ} N_{AE}} \sum_{k=1}^{N_{EQ}} \sum_{j=1}^{N_{AE}} \Theta(r - |x_k - x_j|) \Theta(\tau - |t_k - t_j|) \quad (1.28)$$

where  $N_{AE}$  is the number of peaks of AE activity registered in site, and in a defined time window,  $N_{EQ}$  is the number of earthquakes recorded in the surrounding area during the same time window, and  $\Theta$  is the step function of Heaviside ( $\Theta(x) = 0$  if  $x \leq 0$ ,  $\Theta(x) = 1$  if  $x > 0$ ). The index  $k$  refers to the recorded seismic events  $\{x_k, t_k\}$ , while the index  $j$  refers to the recorded AE events  $\{x_j, t_j\}$ .

Therefore, between all possible pairs of recorded AE and seismic events, the sum expressed by the integral of Grassberger-Procaccia can be calculated for those having the epicentral distance  $|x_k - x_j| \leq r$  and the temporal distance  $|t_k - t_j| \leq \tau$ .

Hence,  $C(r, \tau)$  is the probability of occurrence of two events, an earthquake and an AE event, whose mutual spatial distances are smaller than  $r$  and mutual temporal distances are smaller than  $\tau$ .

Note that, in order to evaluate Eq.(1.28), the numbers of  $N_{AE}$  and  $N_{EQ}$  are not required to assume the same value, and that  $x_j$  corresponds to the geographic position of the monitoring site.

Anyway, this approach does not consider the chronological order of the two types of event. Since the AE time series and the earthquake sequences are closely intertwined in the time domain, the problem of the predictive ability of the AE peaks is still open. The records of AE could be both the consequences of the progressive development of micro-damage, or the effect of widespread micro-seismicity. Therefore, a probabilistic analysis can be carried out discriminating between the AE events prior to the earthquake, which are precursors, and the AE following the earthquake, which are aftershocks. This analysis can be performed adopting a modified correlation integral (Carpinteri et al., 2007c):

$$C_{\pm}(r, \tau) \equiv \frac{1}{N_{EQ}N_{AE}} \sum_{k=1}^{N_{EQ}} \sum_{j=1}^{N_{AE}} \Theta(r - |x_k - x_j|) \Theta(\tau - |t_k - t_j|) \Theta(\pm(t_k - t_j)), \quad (1.29)$$

where "+" and "-" in the function are used to take into account that the AE events could be respectively seismic precursors and aftershocks.

In this way, the function  $C^+(r, \tau)$  gives the probability that a peak of AE, detected at a certain time, will be followed by an earthquake in the subsequent days within a radius of  $r$  kilometers from the AE monitoring site. Varying the thresholds  $r$  and  $\tau$  in Eq. (1.29), two cumulative probability distributions can be constructed, one for each condition (sign "+" or "-") and then the corresponding probability density functions can be derived and represented.

## **2 Ductile and Brittle Materials: Damage and Failure Characterization**

### **2.1 Introduction: Ductile and Brittle Materials**

Structural materials subjected to loading are traditionally catalogued into two distinct categories: ductile and brittle materials. Whereas the former show large portions of the  $\sigma(\epsilon)$  diagram that are not linear, before they reach the fracture point, the latter break suddenly, when the response is still substantially elastic and linear (Figure 2.1a). This is an idealized case that requires a perfect crystalline lattice with a preexisting crack or notch to concentrate the applied stress.

The majority of engineering materials, however, are characterized by a quasi-brittle behavior that shows a non linear segment of the stress-strain curve that precedes the failure of the material (Figure 2.1b) (Carpinteri, 1986; Lemaitre and Chaboche, 1990; Krajcinovic, 1996; Turcotte et al., 2003).

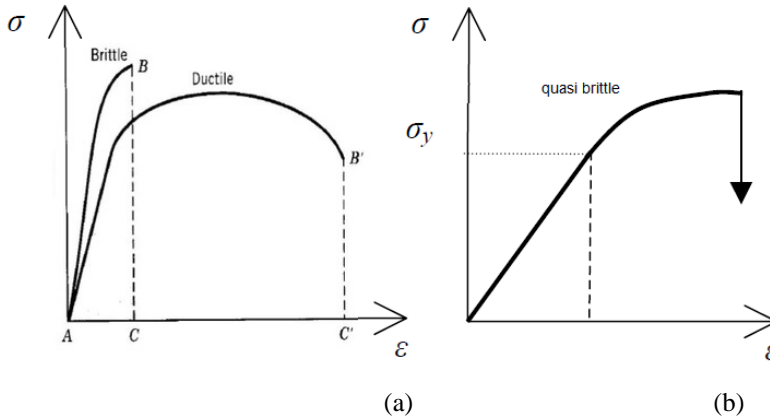


Figure 2.1: (a) brittle and ductile behavior; (b) quasi-brittle behavior.

The differences in behavior depend to a great extent upon the microscopic mechanisms of damage and fracture. In metal alloys, for instance, sliding takes place between the planes of atoms and crystals which gives rise to a behavior of plastic and ductile kind, with considerable permanent deformations. In concrete and rock, on the other hand, the microcracks and debondings between the granular components and the matrix can extend to form a macroscopic crack that splits the structural element suddenly into two parts.

It is not always easy to determine the microscopic magnitude of the damage mechanisms. It may present very different dimensions according to the nature of the mechanisms themselves and the heterogeneity of the material. In crystals, damage occurs at an atomic level, with vacancies and dislocations; in metal alloys, cracks spread at an intergranular level; and in concrete the cracking occurs at the interface between the aggregates and the cement matrix.

## **2.2 Damage and Failure Characterization of Structural Materials**

Damage and failure are complex processes involving wide ranges of time and length scales, from the micro to the structural scale. They are governed by the nucleation, growth and coalescence of microcracks and defects, eventually leading to the final collapse, and to the loss of the classical mechanical parameters, such as nominal strength, dissipated energy density and deformation at failure, as material properties (Carpinteri et al., 2012a). Furthermore, the collapse mechanism is strongly related to the cracking pattern developing during the loading process. It changes from crushing, for very stocky specimens, to shear failure characterized by the formation of inclined slip bands for intermediate values of slenderness, to splitting for very slender specimens.

According to experimental evidences (Kotsovos, 1983; Van Mier, 1984), the post peak phase is characterized by a strong strain localization, independently of the collapse mechanism. Consequently, in the softening regime, energy dissipation takes place over an internal surface rather than within a volume, both in the tension and compression behavior.

According to these evidences, the Overlapping Crack Model (OCM) has been proposed by Carpinteri (Carpinteri et al., 2009a) for modeling the compressive behavior of concrete-like materials. Such a model, dual to the Cohesive Crack Model (CCM) routinely adopted for quasi-brittle materials in tension, assumes a stress vs. displacement (fictitious interpenetration) law as a material property for the post peak behavior, to which corresponds an energy dissipation over a surface. This simple model has permitted to explain the well-known size and slenderness

effects on the structural ductility, characterizing the mechanical behavior of concrete-like materials subjected to uniaxial and eccentric compression tests (Carpinteri et al., 2009a; Carpinteri et al., 2011a).

The overlapping crack model is very effective in describing the overall behavior of specimens in compression, without going into the details of the cracking pattern, as well as in determining the amount of energy dissipated during the complete loading process. On the other hand, more information on the modalities of energy release and the development of cracking patterns can be obtained on the basis of the acoustic emission (AE) monitoring technique. As a matter of fact, cracking is accompanied by the emission of elastic waves which propagate within the bulk of the material. These waves can be received and recorded by transducers applied to the surface of structural elements. This technique, originally used to detect cracks and plastic deformations in metals, has been extended to studies in the field of masonry, rocks and concrete, where it can be used for the diagnosis of structural damage phenomena (Ohtsu, 1996; Carpinteri et al., 2007d). Recently, AE data have been interpreted by means of statistical and fractal analysis (Carpinteri et al., 2007d), showing that the energy release, proportional to the cumulative number of AE events, is a surface-dominated phenomenon. Analogously, also the localization of cracks distribution within the specimen volume by means of the AE technique has physically confirmed the localization of the energy dissipation over preferential bands and surfaces during the damage evolution (Weiss and Marsan, 2003; Carpinteri et al., 2008a; Carpinteri et al., 2008b).

## 2.3 Theoretical Models

### 2.3.1 Uniaxial Tensile

In a uniaxial tensile test carried out on a specimen of ductile material, for instance, low carbon steels (Figure 2.2a), let  $A_0$  be the area of the initial cross section in the middle zone of the bar, and  $l_0$  the initial distance between the sensors glued at two distinct points of the middle zone.

The loading process can be controlled by the external force  $F$  or by the variation in distance  $\Delta l$ . In the second case, it is possible to investigate the behavior of the material beyond the point of ultimate strength. Beyond this point, in fact, the tangential stiffness becomes negative and, to positive increments of displacement  $\Delta l$ , there correspond negative increments of the force  $F$ . This is due to the phenomenon of *plastic transverse contraction* or *necking* (Figure 2.2b).

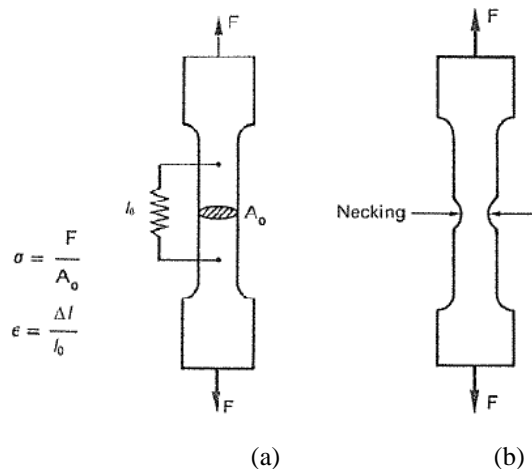


Figure 2.2: (a) uniaxial tensile test; (b) necking phenomenon.

The positive slope of the softening branch may be justified not only by considering the dissipated energy (represented by the area under the curve  $\sigma(\varepsilon)$ ), but also by analytical derivation of the function  $\varepsilon(\sigma)$ . In the post-peak regime, we have (Figure 2.3):

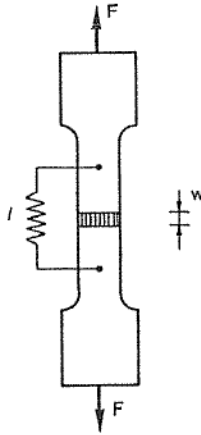


Figure 2.3: post-peak regime scheme.

$$\varepsilon = \frac{\Delta l}{l_0} = \frac{\varepsilon_{el} l_0 + w}{l_0} \quad (2.1)$$

where  $\Delta l$  is the variation in distance between the two sensors,  $w$  is the opening (or width) of the crack and  $\varepsilon_{el}$  indicates the specific longitudinal dilation of the undamaged zone:

$$\varepsilon_{el} = \sigma/E \quad (2.2)$$

From equation (2.1) we then have:

$$\varepsilon = \frac{\sigma}{E} + \frac{1}{l_0} w(\sigma) \quad (2.3)$$

and deriving with respect to  $\sigma$ :

$$\frac{d\varepsilon}{d\sigma} = \frac{1}{E} + \frac{1}{l_0} \frac{dw}{d\sigma} \quad (2.4)$$

This derivate, and consequently also the inverse  $d\sigma/d\varepsilon$ , is greater than zero for:

$$l_0 > E \left| \frac{dw}{d\sigma} \right| \quad (2.5)$$

It follows that there are portions of softening having a positive slope for:

$$l_0 > E / \left| \frac{d\sigma}{dw} \right|_{max} \quad (2.6)$$

therefore, when the distance  $l_0$  is higher than the ratio between the elastic modulus and the maximum slope of the cohesive law.

### 2.3.2 Uniaxial compression

The overlapping crack model proposed by Carpinteri (Carpinteri et al., 2009a) describes the inelastic deformation due to material damage in the post-peak softening regime by means of a fictitious interpenetration of the material, while the bulk material undergoes an elastic unloading. Such a behavior is described by a couple of constitutive laws in compression, in close analogy with the cohesive crack model: a stress vs. strain relationship for the undamaged material (Figure 2.4a), and a stress vs. displacement (fictitious overlapping) relationship describing the material crushing and expulsion (Figure 2.4b). The latter law describes how the stress in the damaged material decreases by increasing the interpenetration displacement, up to a residual value  $\sigma_r$ , is reached, to which corresponds the critical value for displacement,  $w_{cr}$ . The area below the stress vs. overlapping displacement curve of Figure 2.4b represents the crushing energy,  $\mathcal{G}_C$ , which can be assumed, under certain hypotheses, as a size-independent material property.

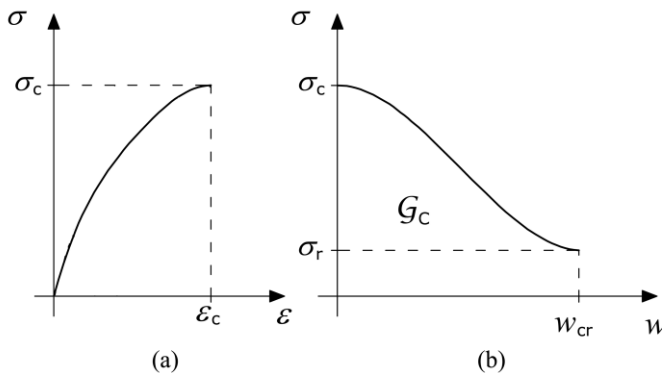


Figure 2.4: Overlapping Crack Model: (a) pre-peak stress vs. strain diagram; (b) post-peak stress vs. interpenetration law.

According to the overlapping crack model, the mechanical behavior of a specimen subjected to uniaxial compression (Figure 2.5a) can be described by three schematic stages.

1. A first stage where the behavior is mainly characterized by the elastic modulus of the material: a simple linear elastic stress-strain law can be assumed, or even more complicated nonlinear relationships, taking into account energy dissipation within the volume due to initiation and propagation of microcracks (Figure 2.5b). By approaching the compressive strength, such microcracks interact forming macrocracks, and, eventually, localizing on a preferential surface.
2. During the second stage, after reaching the ultimate compressive strength,  $\sigma_c$ , the inelastic deformations are localized in a crushing band. The behavior of this zone is described by the softening law shown in Figure 2.4b, whereas the remaining part of the specimen still behaves elastically (Figure 2.5c). The displacement of the upper side can be computed as the sum of the elastic deformation and the interpenetration displacement  $w$ :

$$\delta = \varepsilon l + w \text{ for } w < w_{cr}, \quad (2.7)$$

where  $l$  is the specimen length. Both  $\varepsilon$  and  $w$  are functions of the stress level, according to the corresponding constitutive laws shown in Figure 2.4. While the crushing zone overlaps, the elastic zone expands at progressively decreasing stresses.

3. When  $\delta \geq w_{cr}$ , in the third stage, the material in the crushing zone is completely damaged and is able to transfer only a constant residual stress,  $\sigma_r$  (Figure 2.5d).

As a result, very different global responses in the  $\sigma$ - $\delta$  diagram can be obtained by varying the mechanical and geometrical parameters of the sample. In particular, the softening process is stable under displacement control, only when the slope  $d\delta/d\sigma$  in the softening regime is negative (Figure 2.6a). A sudden drop in the load bearing capacity under displacement control takes place when the slope is infinite, (Figure 2.5b). Finally, the snap-back instability is avoided, (Figure 2.6c), if the loading process is controlled by means of the localized interpenetration or the circumferential strain, the slope  $d\delta/d\sigma$  of the softening branch being positive. Analogously to quasi-brittle materials subjected to tension, the stability of the overall behavior of specimens in compression depends on geometrical (size and slenderness) and mechanical parameters (crushing energy, compressive strength and ultimate strain). In accordance with previous studies proposed by the authors (Carpinteri et al., 2011a), a catastrophic softening (snap-back) occurs when:

$$B = \frac{s_E}{\varepsilon_c \lambda} \leq \frac{1}{2.3}, \quad (2.8)$$

where  $\lambda = l/d$  is the specimen slenderness,  $\varepsilon_c$  is the elastic strain recovered during the softening unloading, and

$$s_{E,c} = \frac{G_c}{\sigma_c d}, \quad (2.9)$$

is the energy brittleness number in compression, proposed by Carpinteri (Carpinteri et al., 2011a).

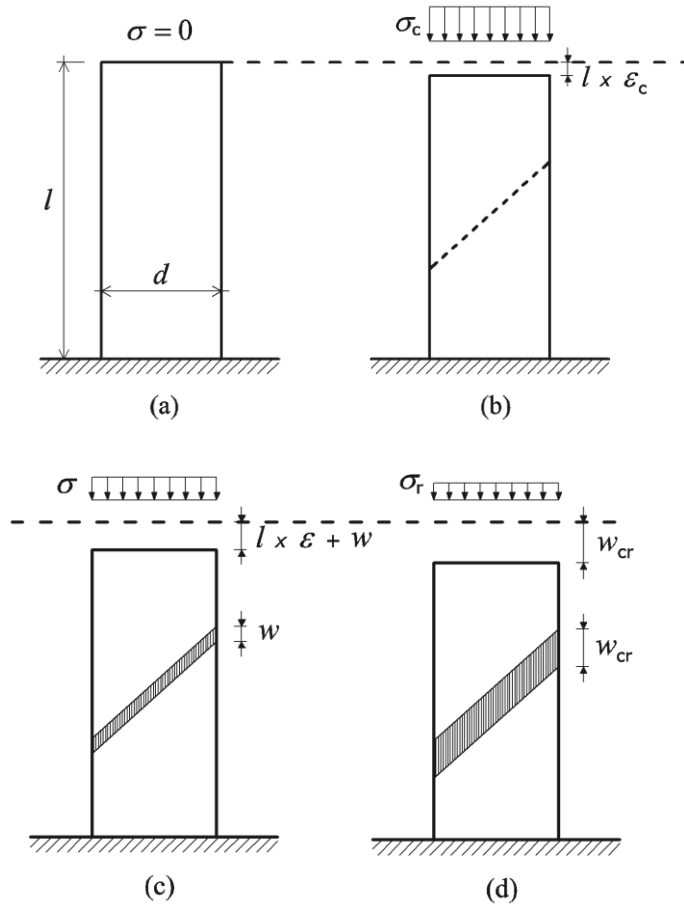


Figure 2.5: Subsequent stages in the deformation history of a specimen in compression.

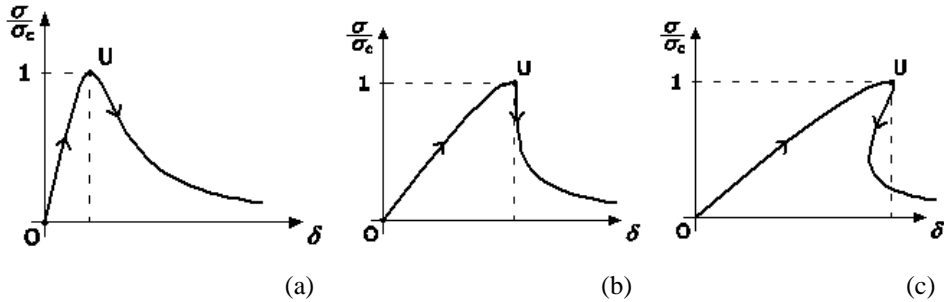


Figure 2.6: Stress vs. displacement response of a specimen in compression: (a) normal softening; (b) vertical drop; (c) catastrophic softening (snap-back).

However, the overlapping crack model, considered as a scale-invariant constitutive model, is no longer valid when the collapse mechanism significantly changes. In this case, the cracking pattern and the amount of energy dissipation also change significantly. As an example, the shear collapse mechanism determines an high energy dissipation due to friction phenomena spread within the specimen volume. On the contrary, the splitting failure, typical of slender specimens, gives rise to a lower energy dissipation, due to the propagation of a main longitudinal tensile crack. The stability of the compression phenomenon is still governed by Eq. (2.8), although the crushing energy depends on the failure mechanism.

### 2.3.3 Three point bending

From a theoretical point of view, the three-point bending test of plain concrete-like beams can be described by means of the cohesive crack model. A linear-elastic behavior is assumed for the beam up to the maximum tensile stress in the central cross section, when the ultimate strength is reached. Then, a cohesive crack starts to propagate from the bottom to the extrados of the beam, whereas the rest of the body exhibits an elastic unloading. However, due to the complexity of the process, only the initial linear elastic behavior and the limit case of central cross section completely cracked can be analytically studied (Figure 2.7) (Carpinteri, 1989). More in details, a linear load vs. deflection relationship is obtained for the former phase, whereas a more complex curve characterizes the post-peak softening phase (Figure 2.8). Analogously to the compression test, the stability of the loading process is governed by a nondimensional parameter. Unstable behavior and catastrophic events are expected when (Carpinteri, 1989):

$$\frac{S_{E,t}}{\varepsilon_u \lambda} \leq \frac{1}{3}, \quad (2.10)$$

where  $\lambda = l/d$  is the beam slenderness,  $\varepsilon_u$  is the ultimate strain in tension, and  $S_{E,t}$  is the energy brittleness number in tension, proposed by Carpinteri (Carpinteri, 1989). The system is brittle for low brittleness number, high ultimate strain and large slenderness (Figure 2.8).

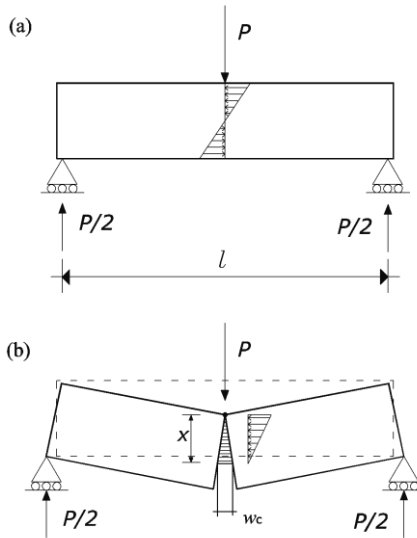


Figure 2.7: Three-point bending geometry: (a) linear elastic phase; (b) limit situation of complete fracture with cohesive forces.

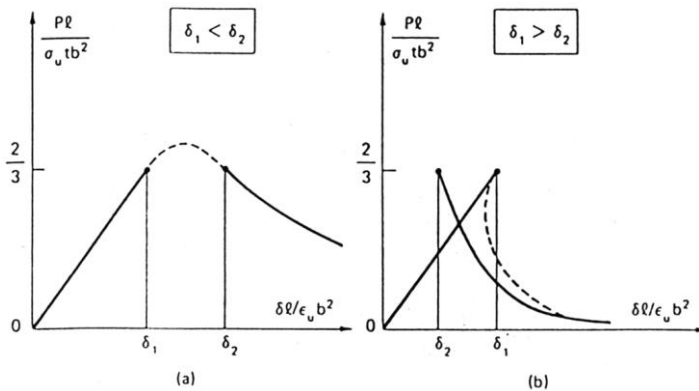


Figure 2.8: Load–deflection diagrams: (a) ductile; (b) brittle condition ( $\delta_1 = \lambda^3/6$ ;

$$\delta_2 = S_{E,I} \lambda^2 / 2 \epsilon_u).$$

### 2.3.3.1 The Cohesive Crack Model

The Cohesive Crack Model (Carpinteri, 1985; Carpinteri, 1989) is used for the study of the ductile-brittle transition and for instability in concrete during tension and bending.

The crack is considered divided in two parts (Figure 2.9): a real crack, identified by the two fracture surfaces that are not able to transfer stresses; and a fictitious crack, in which the stresses transmission is function of the distance between the two faces, still below the limit  $w_{cr}^t$ .

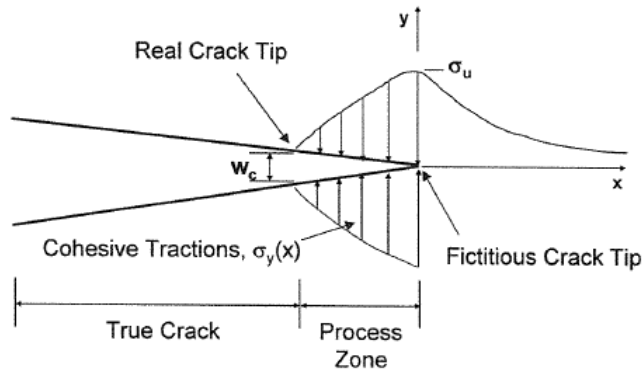


Figure 2.9: Cohesive Crack Model.

The constitutive law used for the nondamaged zone is a  $\sigma$ - $\varepsilon$  linear-elastic relationship up to the tensile strength  $\sigma_u$ . In the process zone, the cohesive stresses are considered to be decreasing functions of the crack opening  $w^t$ , as follows:

$$\sigma = \sigma_u \left( 1 - \frac{w^t}{w_{cr}^t} \right) \quad (2.11)$$

where  $w^f$  is the crack opening;  $w_{cr}^f$  is the critical value of the crack opening corresponding to the condition  $\sigma = 0$  ( $w_{cr}^f \approx 0.1$  mm); and  $\sigma_u$  is the tensile strength of concrete.

For a concrete beam subjected to three point bending test, it is necessary to simulate the Mode I crack propagation with the cohesive model.

In mode I problems, the fracture trajectory is known a priori, so it is possible to create a finite elements pattern that provide  $n$  pairs of nodes disposed along the maximum development of the crack (Figure 2.10).

A discrete form of the elastic equations governing the mechanical response of the beam is herein introduced in order to develop a suitable algorithm for the analysis of intermediate situations where both fracturing and crushing phenomena take place. In this scheme, cohesive stresses are replaced by equivalent nodal forces by integrating the corresponding tractions over each finite element size.

The crack opening, in correspondence of the  $n$  nodes, is given by:

$$\{w^t\} = [K]\{F\} + \{C\}P \quad (2.12)$$

where:  $\{w\}$  = vector of the crack openings;

$[K]$  = matrix of the coefficients of influence ( $F_i = 1$ );

$\{F\}$  = vector of the  $n$  cohesive closing forces;

$\{C\}$  = vector of the coefficients of influence ( $P = 1$ ).  $P$  is the external load.

The coefficients of influence,  $[K]$ , present the physical dimension of a stiffness and are computed a priori with a finite element analysis by applying a unitary displacement to each of the nodes shown in Figure 2.10.

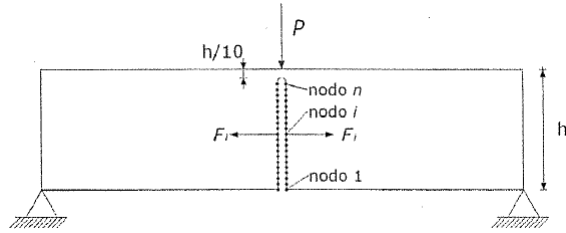


Figure 2.10: nodes of the finite elements pattern disposed along the crack propagation line.

When the process zone is absent (Figure 2.11a), the following equations can be considered:

$$F_i = 0, \quad \text{for } i = 1, \dots, (k-1), \quad (2.13a)$$

$$w_i = 0, \quad \text{for } i = k, \dots, n. \quad (2.13b)$$

Equations (2.12) and (2.13) constitute a linear algebraic system of  $(2n)$  equations and  $(2n)$  unknowns, namely,  $\{F\}$  and  $\{w\}$ .

When the process zone is present (Figure 2.11b), between nodes  $j$  and  $1$ , the following equations can be considered:

(1) in correspondence of the nodes with  $w > w_c^t$  (real crack):

$$F_i = 0, \quad \text{for } i = 1, 2, \dots, (j-1); \quad (2.14a)$$

(2) in correspondence of the nodes with  $0 < w < w_c^t$  (fictitious crack):

$$F_i = F_{t,u} \left( 1 - \frac{w_i^t}{w_c^t} \right), \quad \text{for } i = j, \dots, (m-1); \quad (2.14b)$$

where  $F_{t,u} = \sigma_{t,u} t \Delta x$ , with  $t$  specimen thickness and  $\Delta x$  the distance between two next nodes.

(3) in correspondence of the first node with  $w=0$  (edge of fictitious crack):

$$F_m = F_{t,u} \quad (2.14c)$$

$$w_m^t = 0 \quad (2.14d)$$

(4) in correspondence of the remaining nodes with  $w=0$  (not damaged material):

$$w_i = 0, \text{ for } i = (m+1), \dots, n. \quad (2.14e)$$

Equations (2.12) and (2.14) constitute a linear algebraic system of  $(2n+1)$  equations and  $(2n+1)$  unknowns, therefore it is possible to determine step by step  $\{w'\}$ ,  $\{F\}$  and  $P$ .

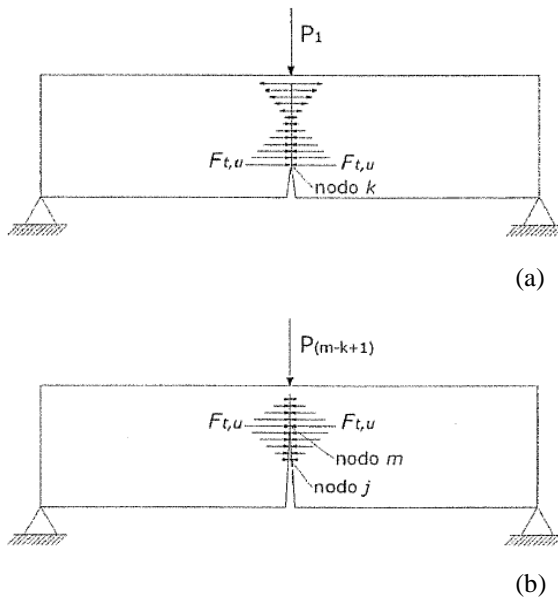


Figure 2.11: forces distribution above the notch: (a) at the first step, (b) at a generic step of the fracture propagation.

Finally, at each step of the algorithm, it is possible to calculate the beam deflection  $\delta$  as follows:

$$\delta = \{C\}^T \{F\} + D_P P \quad (2.15)$$

where  $\{C\}^T =$  vector of the coefficients of influence ( $F_i = 1$ );

$D_P$  is the deflection for  $P = 1$ .

Equations (2.12) and (2.15) allow the fracturing and crushing processes of the midspan cross section to be analyzed by taking into account the elastic behavior of the concrete member. To this aim, all the elastic coefficients are computed a priori using a finite element analysis. Due to the symmetry of the problem, a homogeneous concrete rectangular region, corresponding to half the tested specimen shown in Figure 2.10, is discretized by means of quadrilateral plane stress elements with uniform nodal spacing. Horizontal constraints are then applied to the nodes along the vertical symmetry line (refer to Figure 2.12a). The coefficients entering Eq. (2.12), which relate the nodal force  $F_j$  to the nodal displacement  $w_i$ , have the physical dimensions of a stiffness and are computed by imposing a unitary horizontal displacement to each of the constrained nodes (Figure 2.12b).

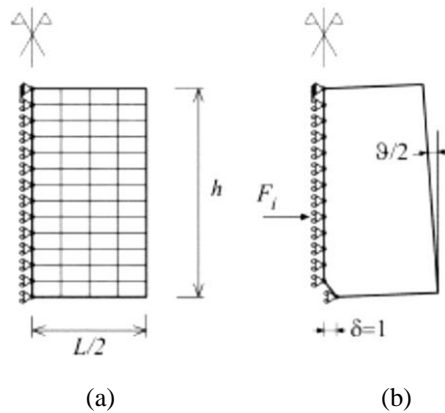


Figure 2.12: (a) Scheme of finite element mesh (b) scheme used for calculation of elastic coefficients.



# **3 Laboratory Tests and Energies Analysis with the AE Monitoring in Brittle and Quasi-brittle Materials**

## **3.1 Introduction: the Acoustic Emission Technique**

The Acoustic Emission (AE) technique is currently used during experimental tests to investigate on the damage evolution in ductile or brittle materials before the final failure (Ohtsu, 1996; Grosse and Ohtsu, 2008). In addition, this non-destructive monitoring method is useful for studying the critical phenomena and to predict the durability and remaining life-time in full-scale structures (Carpinteri et al., 2007b; Carpinteri et al., 2013a).

According to this technique, it is possible to detect the transient elastic waves related to each stress-induced crack propagation event inside a material. These waves can be captured and recorded by transducers applied on the surface of specimens or structural elements. The transducers are piezoelectric sensors that transform the energy of the elastic waves into electric signals. A suitable analysis of the AE waveform parameters (peak amplitude, duration time and frequency) permits to obtain detailed information about the damage evolution, such as the cracking pattern, the released energy, the prevalent fracture mode, and the

achievement of the critical conditions that anticipate the collapse. The last analysis can be performed by calculating the b-value from the Gutenberg-Richter (GR) law (Richter, 1958). Even if two different dimensional scales are involved, the GR law can be carried out in the same way for earthquakes distribution in seismic areas as well as for the structural monitoring by the AE technique (Scholz, 1968; Carpinteri et al., 2008a; Carpinteri et al., 2008b).

The connection between fracture mode and recorded waves depends on different factors like geometric conditions, relative orientations, and propagation distances (Aggelis et al., 2011). The identification of the cracking mode may be done with the AE waves' rise time (which is the time interval between the waves onset and their maximum amplitude), the value of the peak amplitude, and the Average Frequency (AF). The ratio between the rise time (expressed in ms) and the peak amplitude (expressed in V) defines the Rise Angle (RA), as shown in Figure 3.1 (RILEM, 2010a; RILEM, 2010b, and RILEM, 2010c). The peak amplitude can also be expressed in dB by the equation:

$$A [dB] = 20 \cdot \text{Log}_{10} \left( \frac{V}{V_0} \right) \quad (3.1)$$

where  $V$  is the amplitude of the signal in volt, and  $V_0$  is the maximum amplitude of the background noise.

The AF, measured in kHz, is obtained from the AE ring-down count divided by the duration time of the signal. The AE ring-down count corresponds to the number of threshold crossings within the signal duration time (RILEM, 2010a; RILEM, 2010b, RILEM, 2010c).

The fracture mode is then characterized by the shape of the AE waveforms: low RAs and high AFs are typical for tensile crack propagations which consists in

opposite movements of the crack surfaces (Mode I), whereas shear events (Mode II) usually generate longer waveforms, with longer RAs and lower AFs, as shown in Figure 3.1 (Soulioti et al., 2009; Ohno and Ohtsu, 2010; Aggelis, 2011; Aggelis et al., 2012a ; Aldahdooh and Muhamad Bunnori, 2013; Carpinteri et al., 2013c).

The fracture mode criterion is studied by means of the RA and AF relationship for each sensor, as shown in Figure 3.2 (RILEM, 2010b).

Variations in the RA and AF values during the loading process identify a change in the prevalent failure mode of the specimen (Aggelis et al., 2012a; Aggelis et al., 2012b; Carpinteri et al., 2013c).

In general, a decrease in frequency may also be caused by the formation of large cracks during both tensile and shearing processes. As a matter of fact, small cracks occur at the beginning of a damage process, while large fractures take place during the final collapse. Moreover, it is reasonable to assume that high frequency waves propagate through small discontinuities, whereas low frequency ones only can be transmitted through large cracks (Landis and Shah, 1995; Carpinteri et al., 2007a; Carpinteri et al., 2013c).

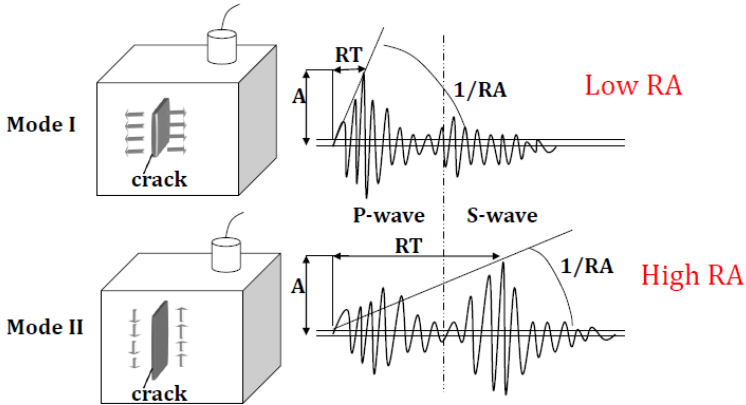


Figure 3.1: Typical waveforms for tensile and shear events. A is the amplitude and RT the rise time (time between the onset and the point of maximum amplitude) of the waveforms (Soulioti et al., 2009; Ohno and Ohtsu, 2010; Aggelis, 2011; Aggelis et al., 2012a; Aldahdoo and Muhamad Bunnori, 2013; Carpinteri et al., 2013c).

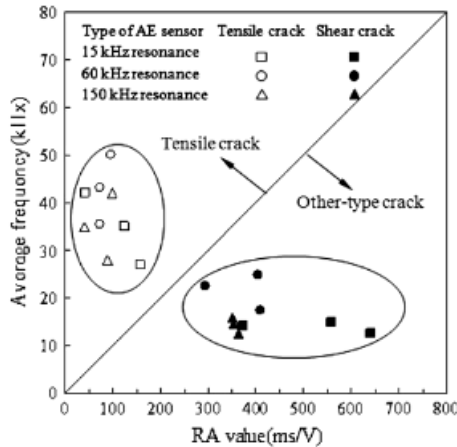


Figure 3.2: Qualification of the damage by AE parameters (RILEM, 2010b).

Another interesting feature of the AE signals is that they can give insights on the process of energy dissipation and emission during the loading process. In this context, experimental analyses have evidenced that the scaling of the cumulative number of AE events by varying the specimen dimension can be profitably used to determine the physical dimension of the damage domain in disordered materials. The total number of AE events at the end of the test, in fact, varies with the specimen size according to a power-law having a non-integer exponent that is directly related to the fractal character of the damage domain (Carpinteri et al., 2007b; Carpinteri et al., 2012). Alternatively, the characterization of the damage domain can be also obtained by means of a statistical analysis of the distribution of AE events related to a single test (Carpinteri et al., 2012). From the viewpoint of energy dissipation and release, the cumulative number of AE events and the energy content of the AE events are usually correlated to the mechanical energy dissipated during the complete failure process, namely fracture energy in tension and crushing energy in compression (Muralidhara et al., 2010). However, recent studies focusing on the catastrophic failure of rock specimens in compression, characterized by snap-back instabilities in the post-peak regime, have suggested that such a correlation is not correct. In the case of very brittle behaviors, the AE energy seems to be correlated to the mechanical energy released during the snap-back instability (Carpinteri et al., 2013b). This particular result can be pointed out only if the complete post-peak branch is captured, e.g. by controlling the test by means of the circumferential expansion instead of the longitudinal deformation.

In this Chapter, the AE parameters acquired during tensile tests, three-point bending tests on notched concrete beams and compression tests on cylindrical specimens are analyzed. These analyses were performed in order to identify the

source localization, the dominant fracture mode and to investigate on the evolution of the released, dissipated and emitted energies during the test and on their correlation.

## **3.2 Experimental tests**

### **3.2.1 Uniaxial tensile tests**

Different re-bars B450C, with a diameter of 18 mm and length of 620 mm, have been tested in a tensile scheme (Figure 3.3a) to obtain detailed information about the fracture localization and the type of cracks. During the test, the steel bars were monitored by the acoustic emission technique. AE signals have been detected by three AE piezoelectric (PZT) transducers, S1, S2 and S3, attached on the steel specimens.

The sensors, sensitive in the frequency range from 80 to 400 kHz for high-frequency AEs detection, are produced by LEANE NET s.r.l. (Italy). The connection between the sensors and the acquisition device is realized by coaxial cables in order to reduce the effects of electromagnetic noise.

The sampling frequency of recording waveforms was set to 1 Msample/s. The data were collected by a National Instruments digitizer with a maximum of 8 channels. The AE signals captured by the sensors, by setting the acquisition threshold level of up to 5 mV, were first amplified up to 40 dB (see Eq. (3.1)), and then processed.

The specimens were subjected to tensile loading up to failure according to EN ISO 6892 recommendation (EN ISO 6892, 2009). To carry out these experiments, an hydraulic press, Walter Bai type, with electronic control was used.

In general, each tensile test was conducted in three subsequent stages. In the first stage it was controlled by stress increments of 15 MPa/s until the yield stress value of the material was reached. Subsequently, the test was controlled by an

imposed strain of 0.16 mm/s up to an elongation equal to 10% of the initial length. In the last stage, which ended with the specimen failure, the imposed deformation was applied by displacement increments of 0.33 mm/s.

In the following, one of the most relevant tests, is reported (Figure 3.3 a,b).

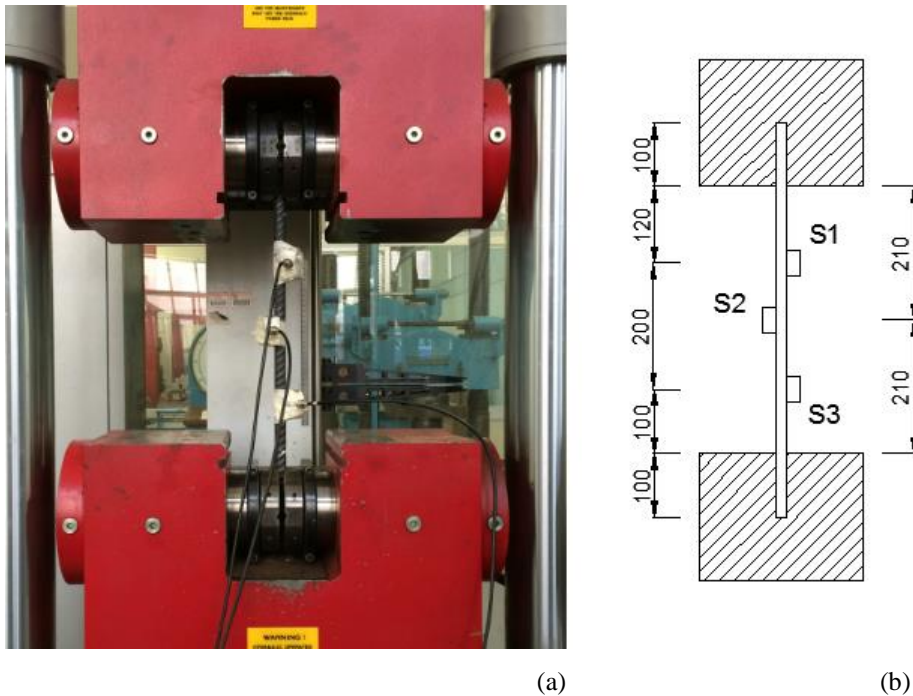


Figure 3.3: Tensile test: (a) experimental test; (b) schematic representation of the experimental setup. S1, S2 and S3 are the sensors applied to detect the AE signals.

The stress vs. strain diagram and the load vs. time diagram are shown in Figure 3.4(a,b), respectively. In the last figure, the cumulated number of AE events, as well as the AE counting rate, are also represented. From a mechanical point of view, at the beginning of the test the response is linear and elastic. Then,

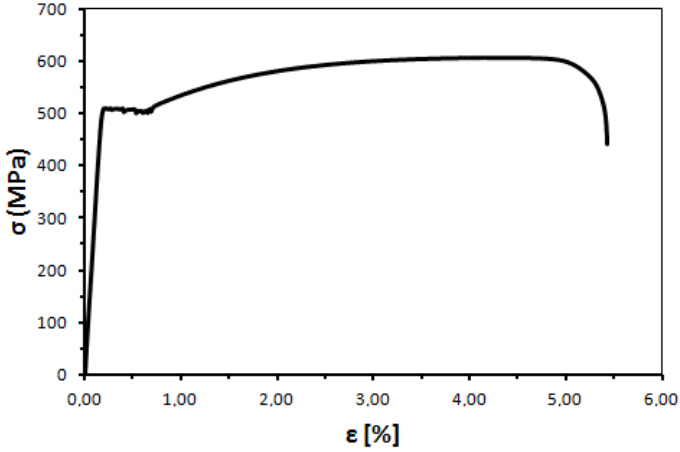
the yield strength limit  $P_y$  is reached, so that dilatation increases by a finite quantity under constant loading. It is followed by the hardening portion of the curve, up to the ultimate strength  $P_u$  and beyond this point the tangential stiffness becomes negative. This is due to the phenomenon of plastic transverse contraction or "necking" which leads to the sudden collapse of the specimen.

The results reported in Figure 3.4b evidence an increase both in the cumulative number of AE events and the AE counting rate at the beginning of the yielding phase and few seconds before the ultimate strength  $P_u$ .

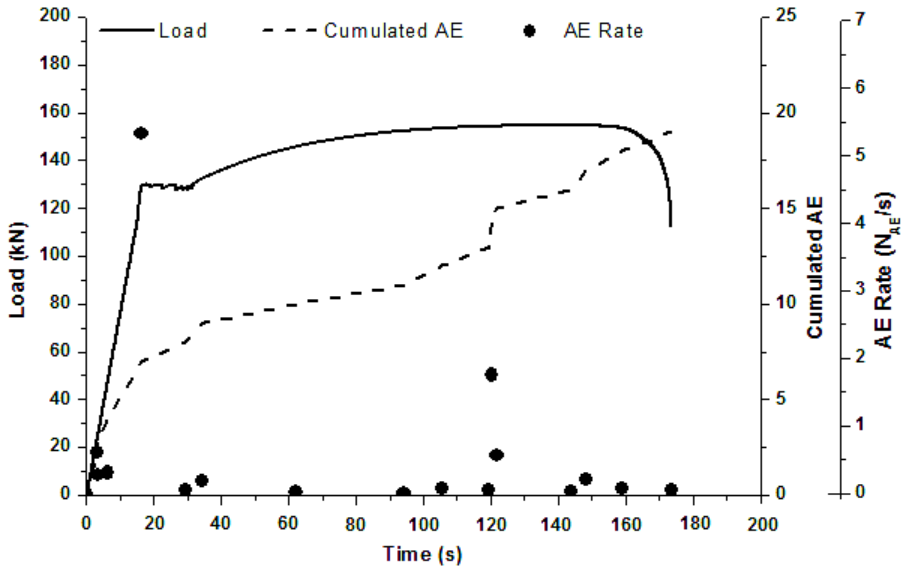
In Table 3.1, the applied loads, as well as the geometrical and mechanical characteristics for the steel specimen are summarized.

Section $S_0$ (mm <sup>2</sup> )	Yield Strength Limit $P_y$ (kN)	Ultimate Strength $P_u$ (kN)	Yielding Stress $\sigma_y$ (MPa)	Stress Peak $\sigma_u$ (MPa)	Elongation at $P_u$ , $\epsilon_u$ (%)	Elongation at Failure $\epsilon_f$ (%)
254.47	129.19	154.73	507.68	608.05	4.28	5.43

Table 3.1: geometrical and mechanical characteristics for the specimen.



(a)



(b)

Figure 3.4: (a): stress vs. strain diagram; (b): load vs. time curve, cumulated AE events and AE counting rate diagram.

### 3.2.1.1 AE source localization

An accurate localization of the AE sources along the specimen has been obtained using the Leane AE acquisition system composed of three PTZ transducers (S1, S2 and S3), whose position on the bar is shown in Figure 3.3b.

When a solid has a dominant dimension with respect to the other two, the problem can be reduced as one-dimensional. As a matter of fact, considering that the re-bar diameter (x, z axes) is negligible compared to its length (y axis), it is a good approximation to consider sensors and source S in-line. In this way the cracks location is distributed only along the longitudinal coordinate (Figure 3.5).

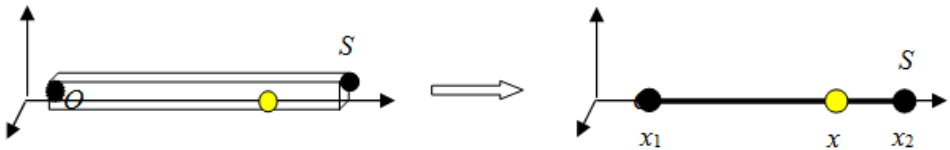


Figure 3.5: Positions of sensors S<sub>1</sub> e S<sub>2</sub> and source S are respectively  $x_1$ ,  $x_2$  and  $x$ .

Only the relative arrival times of the acoustic signals,  $t_1, t_2, t_3$  to each transducer and the positions of the three sensors are known. Therefore, the AE sources are determined by a system of three equations, whose solution gives the wave speed,  $v$ , and the location of the source,  $x$ :

$$\begin{cases} |x - x_1| = v(t_1 - t_0) \\ |x - x_2| = v(t_2 - t_0) \\ |x - x_3| = v(t_3 - t_0) \end{cases} \quad (3.2)$$

From the first equation, we obtain:

$$x = v(t_1 - t_0) + x_1 \quad (3.3)$$

and inserting Eq. (3.3), in the second one of the system, we have:

$$x_1 - x_2 = v(t_2 - t_1) \quad (3.4)$$

Therefore:

$$v = \frac{(x_1 - x_2)}{(t_2 - t_1)} \quad (3.5)$$

Finally, subtracting the latter equation of the system from the second one, it is possible to determine the location of the source,  $x$  as:

$$x = \frac{1}{2}(t_2 - t_3) + \frac{1}{2}(x_2 + x_3) \quad (3.6)$$

Eq. (3.6) can also be calculated for the couples of sensors S1-S2 and S1-S3. In any case, the solution of the system leads to not consider the parameter  $t_0$ , which represents the wave starting time of the AE event, because only the relative arrival times difference between two sensors ( $\Delta t$ ) is necessary.

The AE signals source points localized during the test, are summarized in the Table 3.2. It is assumed that the origin of the reference system Oxyz is the sensor S1.

In addition, from Figure 3.6 it is possible to evaluate the cracking evolution during the tensile loading. The AE sources determined are depicted with black points.

In the elastic phase (Figure 3.6 a), the transducers have localized AE points in correspondence of both the upper and lower jaw. When the yielding trend started up to the end of the test, a high number of acoustic events localization had been identified along the bar (Figure 3.6 b,c,d). A major points concentration was observed between the sensors S2-S3. More in detail, the steel specimen collapsed closer to the sensors S3.

Y (m)	Time (sec)	Y (m)	Time (sec)
-0.155	3.37	0.199	105.52
-0.215	3.48	0.220	119.65
0.347	6.59	0.217	120.30
0.310	16.32	0.190	121.82
0.148	29.59	0.130	143.96
0.170	34.33	0.247	148.47
0.228	62.24	0.127	159.07
0.217	94.30	0.191	173.68

Table 3.2: AE signals source points localized during the loading process.

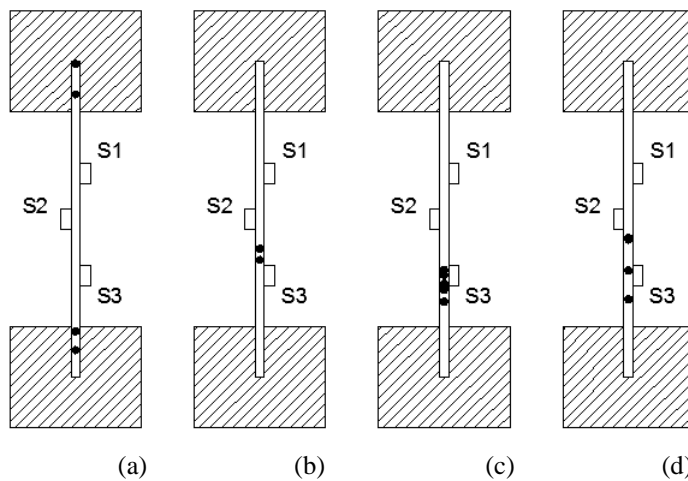


Figure 3.6: AE source localization (a): elastic phase; (b): yielding phase; (c): plastic trend; (d): final collapse.

### 3.2.1.2 Wave propagation velocity, frequencies and wavelength

When you cut a stretched rubber band, it remains subject to rapid fluctuations for a few moments. The same phenomenon occurs in any solid body when it breaks in a brittle way, even if only partially. In the case of the formation or propagation of micro-cracks, such dynamic phenomenon appears under the form of longitudinal waves of expansion/ contraction (tension/compression), in addition to transverse or shear waves. These are generally said pressure waves, or phonons when their particle nature is emphasized, and travel at a speed which is characteristic of the medium, and, for most of the solids and fluids, presents an order of magnitude of  $10^3$  m/s.

In metal alloys, sliding takes place between the planes of atoms and crystals which gives rise to a behavior of a plastic and ductile kind, with considerable permanent deformations. Applying the source location method described in the section 3.2.1.1, the wave propagation speed,  $v$ , for each AE event was also determined. Thus, from the AE location analysis, it was experimentally observed that the wave velocity changed during the different phases of the tensile loading, as shown in Figure 3.7.

In particular at the beginning of the test (elastic phase), the average value of the AE signals velocity in the medium was about 4000 m/s. During the steel yielding, a drop of the wave velocity was observed from about 3500 m/s to about 2500 m/s; while in the plastic phase it changed from about 4000 m/s to about 2500 m/s. Finally, before the collapse is reached, the average AE signals speed remained around 2300 m/s.

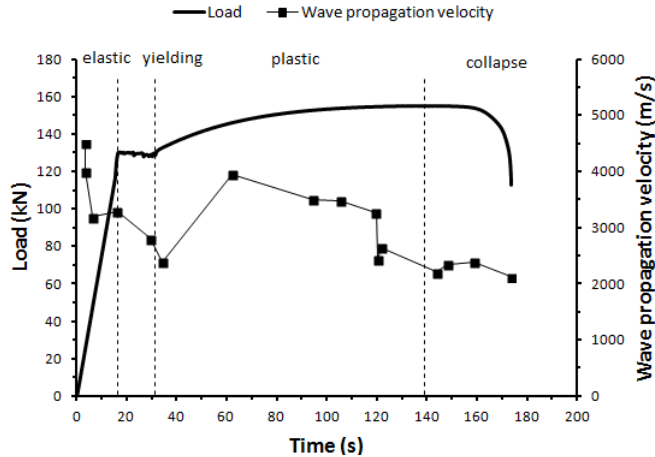
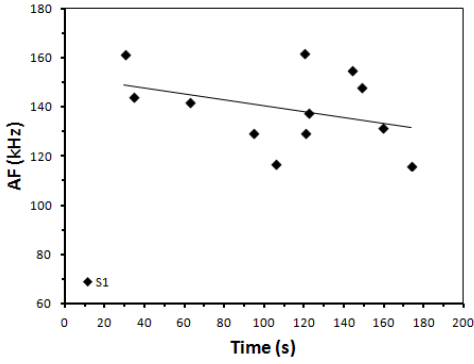


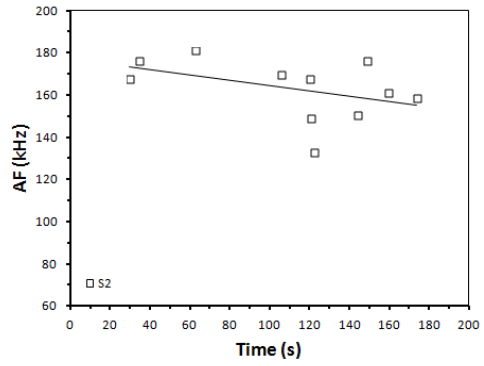
Figure 3.7: load vs. time curve compared with the wave propagation velocity diagram.

In addition, from the AF analysis, a decrease of its values was obtained from yielding up to the end of the test. The AF values related to the elastic phase were not considered due to the friction created between the steel bar and the press jaws. Anyway, a shift in frequencies of about 10% from higher to lower values was observed for each sensor (Figure 3.8 a,b,c).

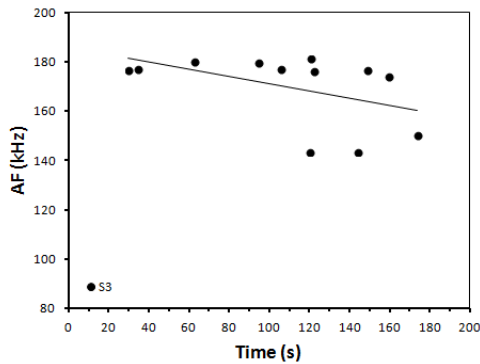
It must be also considered that the wavelength of pressure waves emitted by forming or propagating cracks appears to be of the same order of magnitude of crack size or crack advancement length. The wavelength can not, therefore, exceed the maximum size of the body in which the crack is contained and may vary from the nanometre scale ( $10^{-9}$  metres), for defects in crystal lattices such as vacancies and dislocations, up to the kilometre, in the case of Earth's Crust faults. In fact in solids, whatever their size, the cracks that are formed or propagate are of different lengths, sometimes belonging to different orders of magnitude.



(a)



(b)



(c)

Figure 3.8: AF vs. time diagram for (a): Sensor 1; (b): Sensor 2; and (c): Sensor 3.

In this case, applying the relationship:

$$\lambda = v/f \quad (3.7)$$

and considering the average values of wave propagation speed and frequencies measured during the test, a wavelength of about 0.02 m was obtained.

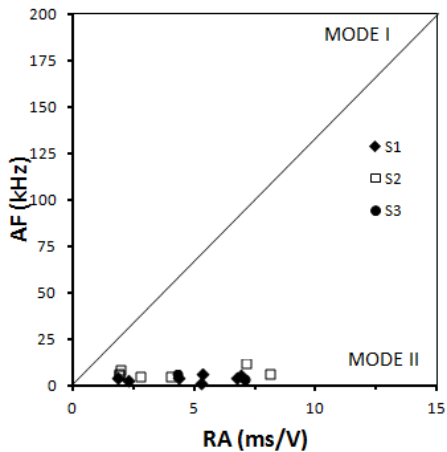
### 3.2.1.3 Identification of the fracture mode

The fracture mode has been studied by means of the relationship between RA and AF values estimated for each sensor.

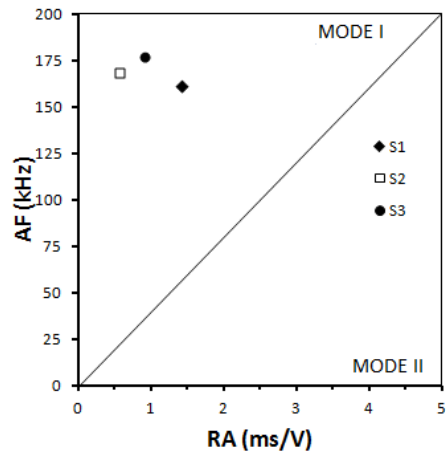
During the elastic phase (about 16 s), rather high RA values and very low frequencies characterized the AE signal events. This is due to the friction created between the steel bar and the press jaws (Figure 3.9 a).

In the yielding and plastic phases, until the ultimate strength  $P_u$  is reached (from about 16 s to about 139 s), a dominant presence of Mode I cracks seems to characterize the damage evolution (Figure 3.9 b,c). Finally, from 139 s up to the end of the test (about 175 s), when the final collapse is reached, the prevalent cracking mode is still the pure opening mode (Figure 3.9d).

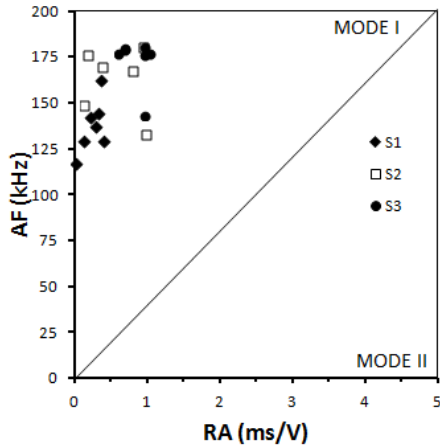
Therefore, the collapse of the specimen is reached by a Mode I type of fracture, even if friction components between the bar and the press jaws characterized the initial stage of the test (Figure 3.9e).



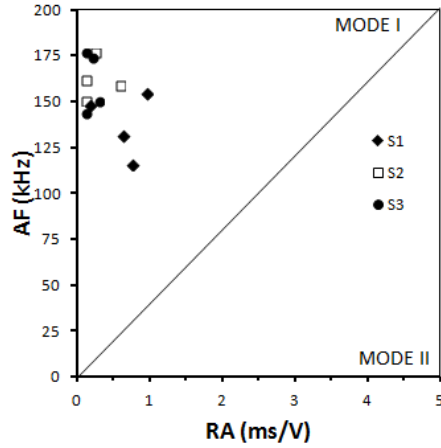
(a)



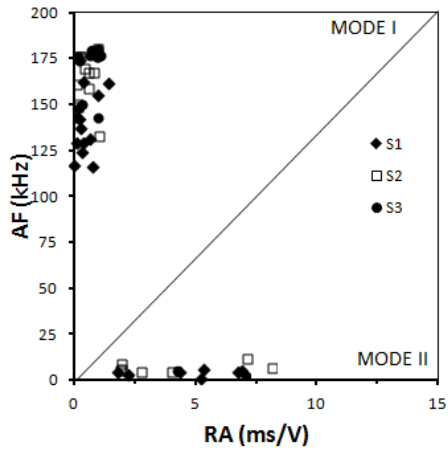
(b)



(c)



(d)



(e)

Figure 3.9: Fracture mode identification by means of the relationship between RA and AF values for a steel specimen under tensile: (a) from 0 to 16 s; (b) from 16 s to 31 s; (c) from 31 s to 139 s, (d) from 139 s up the end of the test; (e) total duration of the test.

### **3.2.2 Three point bending tests (TPB)**

In this section, the AE parameters acquired during three-point bending tests on notched concrete beams are analyzed. These analyses were performed in order to identify the dominant fracture mode and to investigate on the evolution of the released, dissipated and emitted energies during the test and on their correlation.

The AE activity was monitored by two sensors applied for each beam. The sensors were placed at different distances from the notch to evaluate how the transient waves from the same damage event change with the distance between the source and the receiver. As a matter of fact, AE waveform parameters are affected by attenuation and distortion due to propagation through an inhomogeneous medium. A numerical simulation of the mechanical response of the experimental tests was also performed on the basis of the cohesive crack model. This approach has permitted to obtain a detailed description of the crack propagation during the loading test and to evaluate the corresponding step-by-step energy dissipation. Finally, a comparison between the released energy obtained by AE and the dissipated energy calculated by the numerical simulation is shown.

Three plain concrete beams with different dimensions have been tested in a three-point bending scheme (Figure 3.10). The main geometrical parameters are reported in Table 3.3. All the beams were pre-notched after curing for a depth equal to half the overall height.

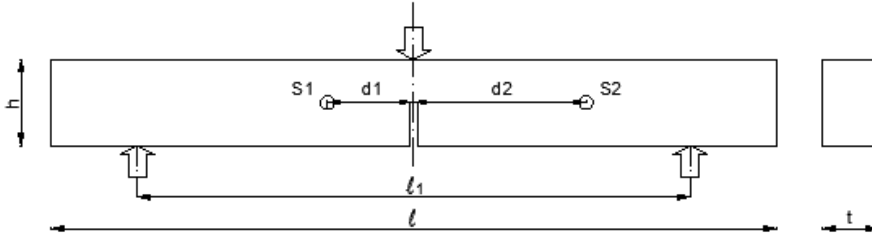


Figure 3.10: Schematic representation of the experimental setup. S1 and S2 are the sensors applied to detect the AE signals.

	SPECIMEN B1	SPECIMEN B2	SPECIMEN B3
$l$ (mm)	840	1190	1450
$h$ (mm)	100	200	300
$t$ (mm)	100	100	150
$l_1$ (mm)	800	1140	1180
$d_1$ (mm)	40	150	200
$d_2$ (mm)	110	300	400

Table 3.3: Main geometrical parameters of the beams.

Three different concrete mixes were selected, one for each beam dimension. In particular, the maximum aggregate size was varied from 15 mm for the smallest beam to 45 mm for the largest one. Correspondingly, the water to cement ratio by mass was varied from 0.63 to 0.53. The nominal average compressive strength is equal to 25 MPa for all the three concrete mixes.

The specimens were subjected to three-point bending tests according to the RILEM Technical Committee TC-50 specifications (RILEM, 1986). The

experimental tests were conducted using a servo-hydraulic MTS testing machine (Figure 3.11). The samples were tested up to final failure by controlling the crack mouth opening displacement (CMOD) with an opening velocity equal to 0.002 mm/s. Moreover, also the vertical deflection ( $\delta$ ) at the centerline of the beams was measured.

During the tests, each specimen was monitored by the AE technique. The AE signals were detected by two piezoelectric (PZT) transducers, S1 and S2, attached on the surface of the concrete specimen (Figure 3.11). The sensors were positioned on the left and right sides of the notch, at increasing distances for each analyzed sample. The distances of each sensor,  $d_1$  and  $d_2$ , are reported in Table 3.3. The sensors, sensitive in the frequency range from 80 to 400 kHz for high-frequency AEs detection, are produced by LEANE NET s.r.l. (Italy). The connection between sensors and acquisition device is realized by coaxial cables in order to reduce the effects of electromagnetic noise.

The sampling frequency of recording waveforms was set to 1 Msample/s. The data were collected by a National Instruments digitizer with a maximum of 8 channels. The AE signals captured by the sensors, setting the acquisition threshold level of up to 5 mV, were first amplified up to 40 dB (see Eq. (3.1)), and then processed.



Figure 3.11: Experimental set up of the three point bending test.

### 3.2.2.1 AE parameters analysis

The AE data acquisition procedure employed during the tests was based on the total number of hits detected by each sensor, but the AE analysis was limited only to the AE events. An hit is one AE transient signal received by a sensor, whereas one event is a couple of AE hits detected from a single source by the two receivers, the spatial coordinates of which are known (RILEM, 2010a). In this way, it is possible to compare each signal captured by the first receiver with the same recorded by the second one, even if they have different distances from the source.

For each beam, the average values of the AE signals parameters recorded by the first sensor have been compared to those of the second sensor.

The load vs. time diagram for the beam with dimensions 840x100x100 mm (Specimen B1) is shown in Figure 3.12. In the same figure, the AFs and the RAs of each AE event (i.e. calculated for each pair of signals, and averaged on the couple of the signals received by the two sensors), as well as the cumulated number of AE events are represented. From a mechanical point of view, the overall behavior is characterized by a softening post-peak branch with negative slope.

The results reported in Figure 3.12 evidence a slight decrease in the AFs by approaching the final stage of the test. Moreover, the phenomenon of the signal attenuation, due to the wave propagation through an inhomogeneous medium, is analyzed by comparing the mean values of the signal amplitudes and the AFs received by the sensors S1 and S2. The sensors were placed at different distances from the mid-span cross-section, where most of the signal sources are localized due to the symmetry of the specimen. The mean value of the AFs is 69.55 kHz and 63.21 kHz for sensor S1 and S2, respectively (Figure 3.13a). Thus, a small shift in the frequencies from higher to lower values is observed, as the distance of the receiver from the source increases. As regards the signal amplitudes, a decrease in the average value between the two sensors is expected, due to damping and scattering effects. The obtained results are reported in Figure 3.13b. The average amplitude recorded by the nearest receiver S1 is 66 dB, whereas a drop of about 1 dB is observed for sensor S2.

The fracture mode was analyzed by means of the relationship between RA and AF values estimated for each sensor, as shown in Figure 3.14. Considering that a slight decrease in the AFs by approaching the final stage of the test is obtained, and that the RA values are all lower than 1 ms/V, a dominant presence of tensile

cracks seems to characterize the damage evolution up to the final collapse (Aggelis et al., 2012b; RILEM, 2010c; Soulioti et al., 2009).

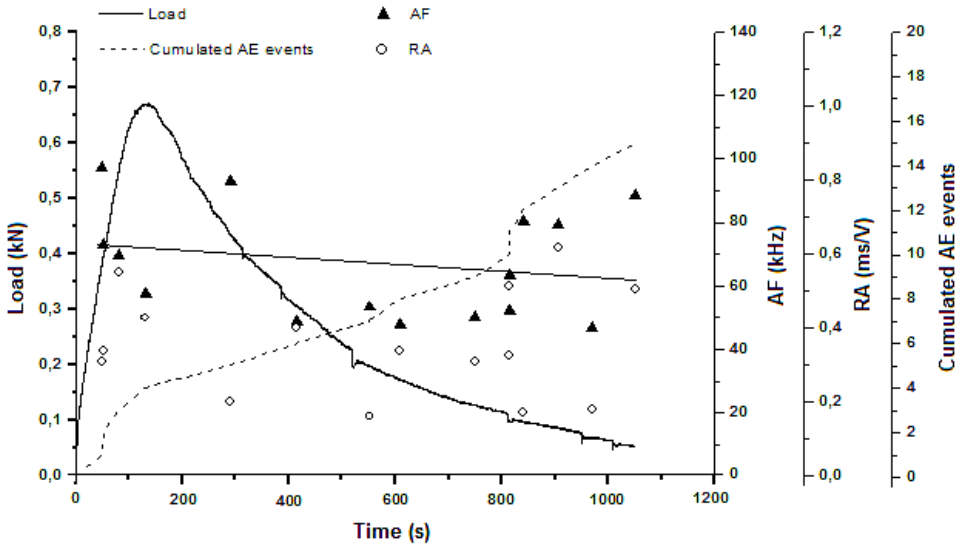


Figure 3.12: Specimen B1 (840x100x100 mm): load vs. time curve, AF and RA values of the detected AE events, and cumulated diagram of the AE events. The straight line represents the linear regression of the AF values during the test.

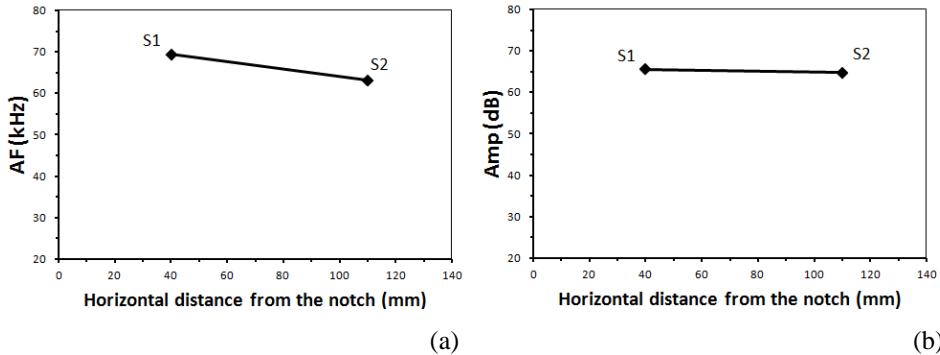


Figure 3.13: Specimen B1 (840 x 100 x 100 mm): (a) mean value of the AFs and (b) average amplitude of the signals detected by the two sensors during the test.

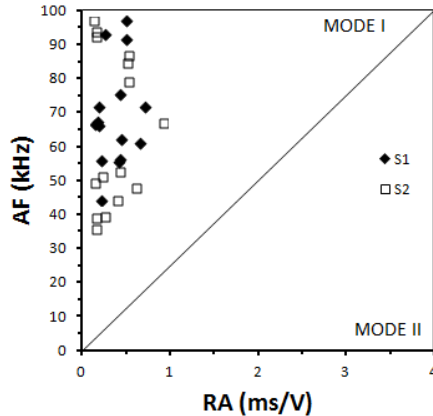


Figure 3.14: Specimen B1 (840x100x100 mm): fracture mode identification by means of the relationship between RA and AF values.

As regards the beam of dimensions 1190x200x100 mm (specimen B2), the load vs. time curve, the values of AF and RA, and the cumulated curve of the AE events are shown in Figure 3.15. The overall mechanical behavior has a similar trend compared to the previous one, even if an increase in the cumulative number of AE events at the end of the test is evidenced.

The average value of AE frequencies slightly decreases during the loading test (Figure 3.15). Analogously to specimen B1, an attenuation of both AFs and amplitudes was obtained by increasing the distance between source location and sensors, as shown in Figure 3.16. The mean value of the AFs is 66 kHz and 51 kHz for sensor S1 and S2, respectively (Figure 3.16a). The value of the average amplitude decreases from 58.7 dB for sensor S1 to 55.2 dB for sensor S2, i.e. with increasing the distance of the sensors with respect to the source (Figure 3.16b).

Considering the relationship between RA and AF values, the cracking mode was studied. Against a slight decrease in the AFs, the RA values are all less than 1 ms/V (Figure 3.17), thus the evolution of damage from the initial notch was dominated by a Mode I crack formation and propagation.

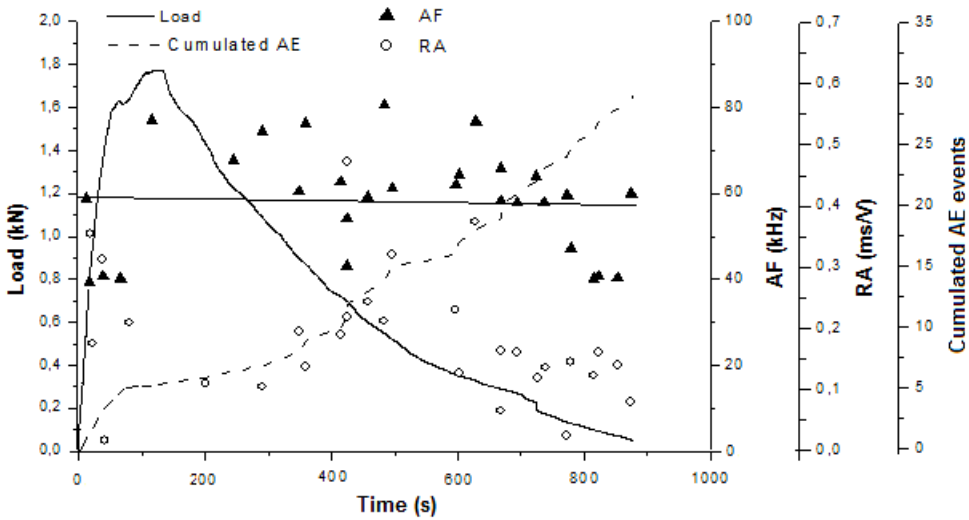


Figure 3.15: Specimen B2 (1190x200x100 mm): load vs. time curve, AF and RA values of the detected AE events, and cumulated diagram of the AE events. The straight line represents the linear regression of the AF values during the test.

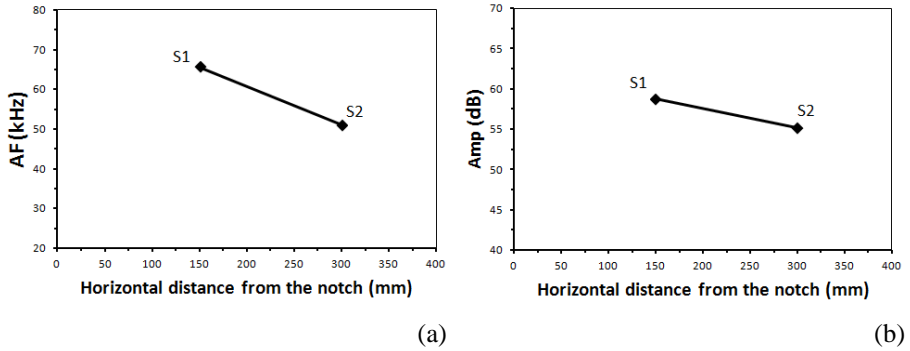


Figure 3.16: Specimen B2 (1190x200x100 mm): (a) mean value of the AFs and (b) average amplitude of the signals detected by the two sensors during the test.

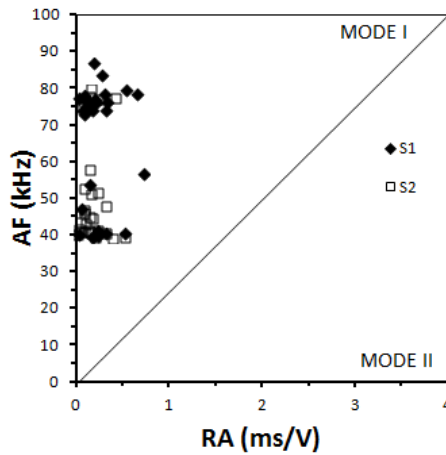


Figure 3.17: Specimen B2 (1190x200x100 mm): fracture mode identification by means of the relationship between RA and AF values.

The results of the three-point bending tests performed on Specimen B3 are reported in Figure 3.18. The cumulative number of AE events at the end of the test is higher than in the previous cases (see Figures 3.12 and 3.15). The AE signals

detected by the two sensors show characteristics similar to those of specimens B1 and B2, although in this case a clear shift in frequencies from higher to lower values was obtained. As a matter of fact, the AE average frequency decreases from 54 kHz, for sensor S1, the one closer to the fracture surface, to 49 kHz for the farther one, S2 (Figure 3.19a). As regards the average amplitude, it decreases from 57.2 dB for receiver S1 to 56.2 dB for S2 (Figure 3.19b).

The diagram of AF vs. RA, for each detected signal, evidences again as the dominant crack modality is opening (Figure 3.20).

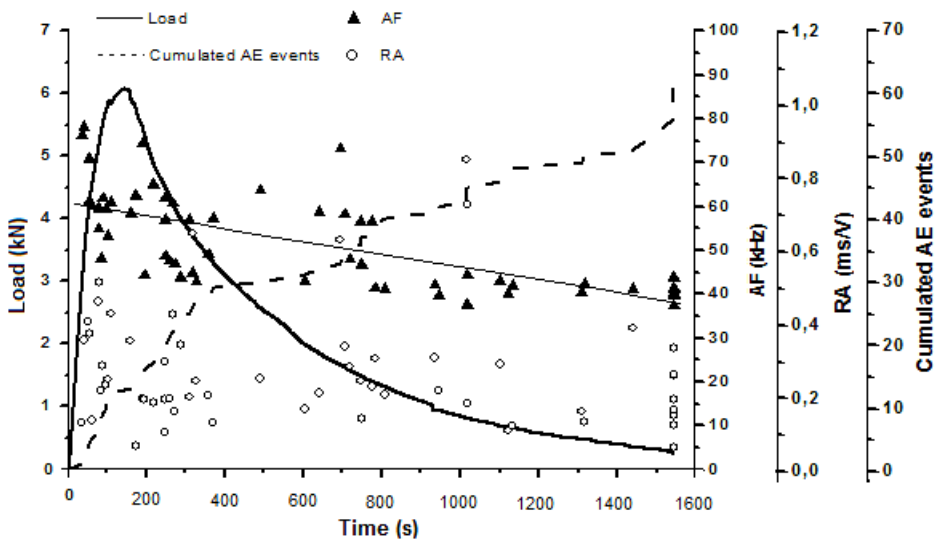


Figure 3.18: Specimen B3 (1450x300x150 mm): load vs. time curve, AF and RA values of the detected AE events, and cumulated diagram of the AE events. The straight line represents the linear regression of the AF values during the test.

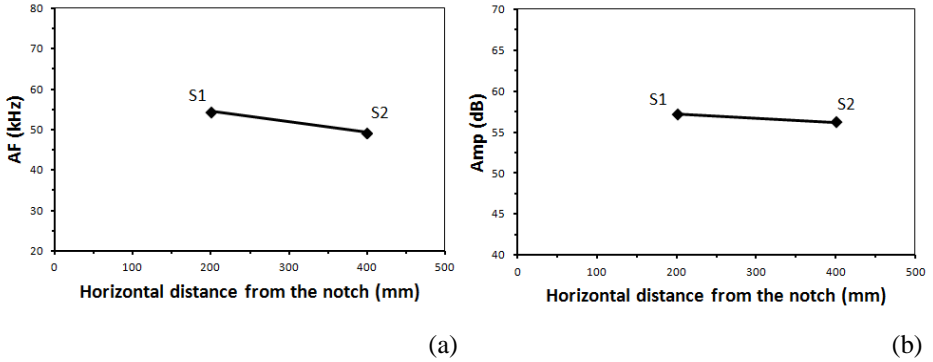


Figure 3.19: Specimen B3 (1450x300x150 mm): (a) mean value of the AFs and (b) average amplitude of the signals detected by the two sensors during the test.

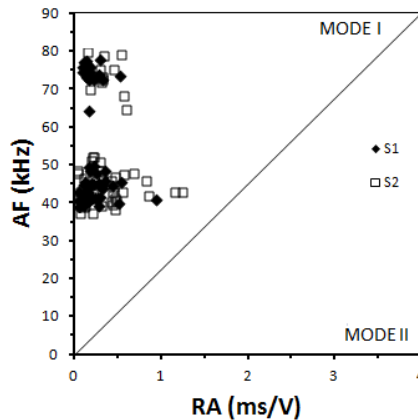


Figure 3.20: Specimen B3 (1450x300x150 mm): fracture mode identification by means of the relationship between RA and AF values.

Finally, the average values of the peak amplitude vs. distance between the acoustic sources and the AE sensor, for the three performed bending tests, are synthesized in Figure 3.21. The considered distances on the three beams range from 40 to 400 mm. Due to the concrete attenuation properties, by increasing the

distance, a shift in amplitudes from 66 dB to 56 dB is observed. From an experimental point of view, a linear decrease proportional to the signals propagation length is observed (the slope of the regression line is equal to 0.029).

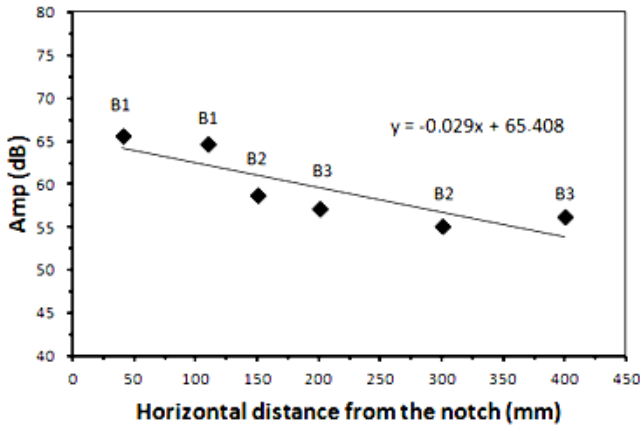


Figure 3.21: Average amplitude values vs. distance between crack surface and AE sensor.

### 3.2.2.2 Dissipated vs. emitted energy

The AE parameters were also analyzed in order to investigate on the evolution of the released, dissipated and emitted energies during the test and on their correlation.

The released energy is the total energy released during the loading process, i.e. the energy spent by the machine to perform the test, the dissipated energy corresponds to the Griffith energy necessary to create the fracture surfaces, and the emitted energy is the energy detected by the AE technique. The mechanical dissipated energy is determined both directly from the experimental

load-displacement curves and by means of a numerical algorithm developed to simulate the step-by-step crack propagation during the loading test on the base of the cohesive crack model. As far as the emitted energy is concerned, its estimation is obtained from the energy of the AE signals detected by the sensors.

Then, the dissipated and the emitted energies were compared on the basis of their cumulative value at the end of the test and their rates during the loading process.

The total mechanical energy dissipated by the fracture process in the considered three-point bending tests was evaluated according to the RILEM Recommendations (RILEM, 1985). The obtained results are reported in Table 3.4, where the corresponding value of the fracture energy, evaluated as the ratio between the total dissipated energy and the ligament area, are also shown. A considerable increase in the fracture energy was evidenced by increasing the specimen size. This is partially due to the well-known scale effects on the toughness of quasi-brittle materials (Carpinteri and Chiaia, 1996), as well as to the variation in the maximum aggregate diameter of the concrete mix with the beam size (see Section 3.2.2). The increase in the maximum aggregate diameter, in fact, increases the tortuosity of the crack path, with a consequent increase in the apparent fracture energy. The combined effect of these two phenomena is confirmed by the fact that the increase in the fracture energy with the specimen size can be described by a power-law having an exponent equal to 0.64 (see the diagram in bi-logarithmic scale shown in Figure 3.22), whereas extended analysis carried out in the past to assess the validity of the fractal approach to describe the size effect on the fracture energy in concrete-like materials have evidenced values for this exponent in the range between 0.20 and 0.30 (Carpinteri and Ferro, 1998).

The energy of the AE signals detected during the tests was also evaluated for the three beams. This energy, in accordance with the RILEM TC 212-ACD Recommendations, was calculated as the waveform envelope area of each signal (RILEM, 2010a). The values of the total emitted AE energy at the end of the three tests are reported in Table 3.4. It is worth noting that, since the evaluation of the AE energy is affected by the phenomenon of signal attenuation, the values have been corrected according to the attenuation law obtained in Figure 3.21. The problem of the signal amplitude attenuation due to distance is to be taken seriously into account especially when large structures are monitored. It can be solved only by arranging several sensors to cover large monitored areas (Carpinteri et al., 2013a). In the same table, the corrected AE energy divided by the ligament area is also reported. As clearly evidenced by the diagrams in Figure 3.22, the AE energy per surface unit decreases by increasing the specimen size, exhibiting, therefore, an opposite trend compared to that of the fracture energy. Such a discrepancy suggests that there is no a direct correlation between the two parameters. In fact, the AE energy is an emitted energy, consequent to a surplus of stored elastic energy with respect to the dissipated one. In this context, it has been recently shown that a large amount of AE energy emission takes place in the case of macrostructural catastrophic failures, such as the collapse of a brittle rock specimen in compression with snap-back instability (Carpinteri et al., 2013b). Obviously, such an energy can be detected only if the entire post-peak path is stably followed, by means of specific experimental techniques. Differently from the compression test analyzed in (Carpinteri et al., 2013b), the TPB tests herein considered are characterized by a normal softening behavior, without overall instabilities. However, even in case of stable macrostructural behavior, local

discontinuities, which are an indication of snap-back or snap-through instabilities, are usually noticed in heterogenous materials such as concrete-like and fiber reinforced materials. Such a local phenomenon, that is evident at a microscale level, is due to the fact that cracks growth in a discontinuous manner, with sudden initiations and arrests of propagation due to the bridging action of the secondary phases as well as by the rise and coalescence of microcracks in the process zone. Such a kind of behavior has been accurately studied from a mechanical point of view by means of numerical and semi-analytical approaches (Carpinteri and Massabò, 1997; Carpinteri and Monetto, 1999). As an example, the normalized stress-strain curve obtained from a numerical simulation with the boundary element method of the fracture evolution of a multicracked solid is shown in Figure 3.23 (adapted from Carpinteri and Monetto, 1999). The initial central cracks produce local amplification followed by local shielding of the stress field around the tip of the edge cracks, leading to a sequence of initiations and arrests of propagation. Each local instability provokes an energy release (dashed areas in Figure 3.23), that can be detected by the AE sensors. The process of crack propagation in concrete is in fact very similar to that herein described due to the presence of microcracks and voids inside the cement matrix, as well as due to the bridging effect exerted by the aggregates. Some of the local instabilities occurring during the post-peak regime of Specimen B1 are evidenced in Figure 3.24. The more pronounced the instabilities are, the higher the released energy and, therefore, the acoustic emission activity, is.

	SPECIMEN B1	SPECIMEN B2	SPECIMEN B3
W (J)	0.59	1.73	5.42
$G_F$ (N/m)	118	173	241
AE Energy (ms*V)	589	930	1494
Corrected AE Energy (ms*V)	589	1038	1712
Corrected AE Energy/Ligament (ms*V/m <sup>2</sup> )	117800	103800	76089

Table 3.4: Total dissipated energy  $W$ , fracture energy  $G_F$ , released AE energy, and AE energy per surface unit for the three beams.

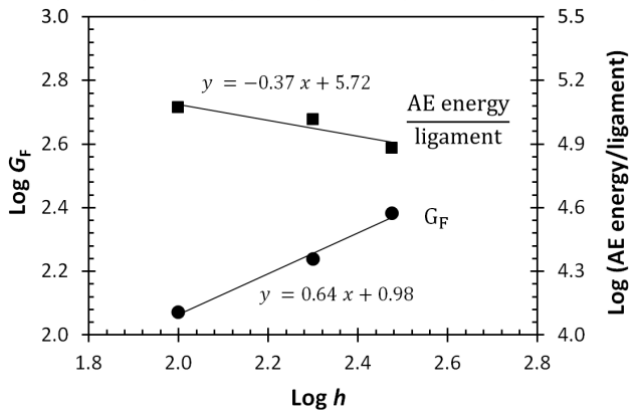


Figure 3.22: Bi-logarithmic scale diagrams of the fracture energy and the AE energy per surface unit vs. the beam height.

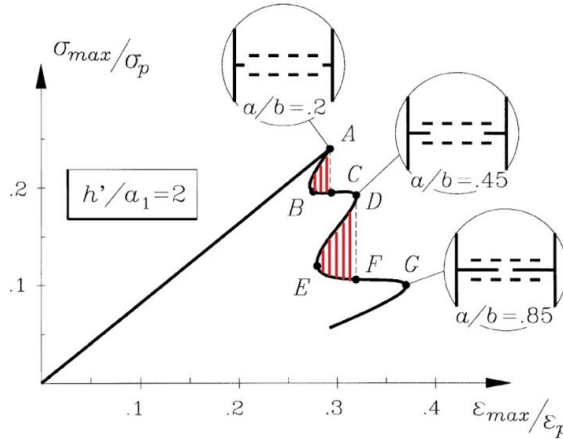


Figure 3.23: Normalized stress-strain diagram consequent to the propagation of edge macrocracks in a homogeneous material plate with pre-existing microcracks (adapted from Carpinteri and Monetto, 1999). "a" is the initial length of the edge cracks, "a<sub>1</sub>" is half the initial length of the internal cracks, "h" is half the distance between the two rows of internal cracks, "b" is the dimension of the plate.

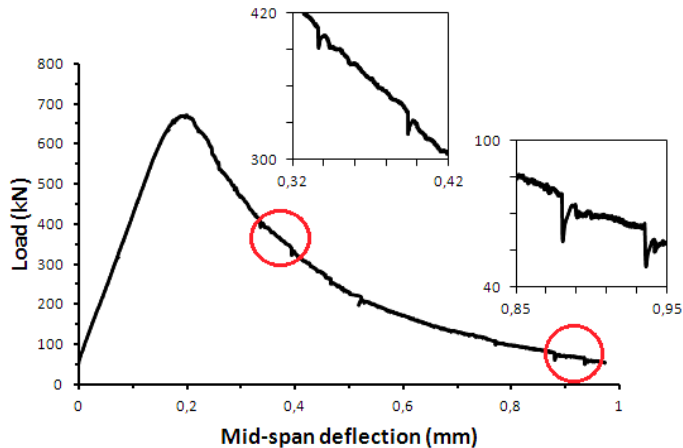


Figure 3.24: Experimental load vs. mid-span deflection curve of Specimen B1, with magnification of some instabilities occurring in the post-peak regime.

### 3.2.2.3 Dissipated and emitted energy rates

The differences between dissipated and emitted energies are herein analyzed on the basis of the evolution of these two quantities over the time, during the progress of the experimental test. To this purpose their rate, defined as the amount of energy per second, has been computed for the three performed tests. As regards the rate of the AE energy, it has been directly derived from the results of the monitoring activity carried out during the tests. On the contrary, the rate of the dissipated energy has been assessed both from the experimental results and by means of an accurate numerical simulation of the fracturing process. In the former case, the evolution of the energy dissipation has been evaluated on the basis of the load vs. time and load vs. displacement curves, according to the following procedure, that is also graphically described in Figure 3.25 a,b:

- 1- the load corresponding to the overcoming of the elastic limit, after which energy dissipation takes place, is estimated in the load vs. displacement curve (Figure 3.25b);
- 2- the point corresponding to the elastic limit is reported into the load vs. time diagram that, starting from the corresponding time value, is subdivided in several parts, one every second (Figure 3.25a);
- 3- the load values corresponding to the subdivisions are reported back into the load vs. displacement curve, where
- 4- the areas representing the energy dissipated for each second are defined by means of segments drawn parallel to the elastic branch. The contribution of the self-weight is also added, by applying a translation to the reference system, as shown in Figure 3.25b.

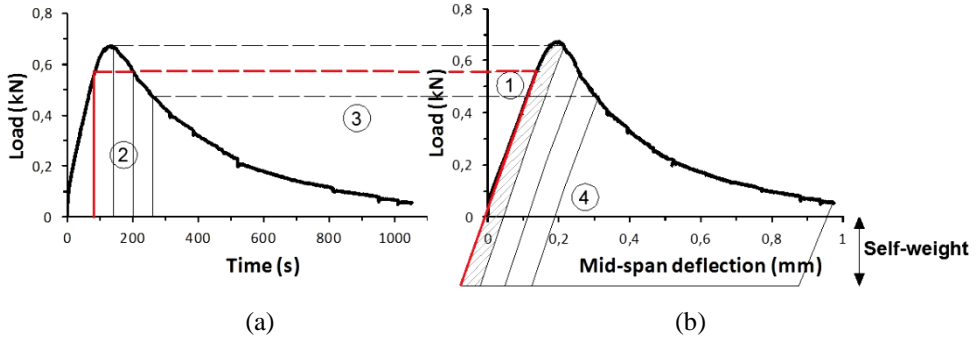


Figure 3.25: Sketch of the procedure followed to compute the dissipated energy rate: (a) load-time and (b) load-displacement diagrams.

In the second proposed approach, the fracturing process is modeled by means of a numerical algorithm based on the cohesive crack model, and the dissipated energy is evaluated in terms of step-by-step variation of the cohesive tractions and of the relative opening displacements along the crack profile. The advantage of such an approach is that the energy dissipation is directly analyzed in relation to the crack propagation process, which is, in fact, the phenomenon responsible for the mechanical energy dissipation. The numerical algorithm originally proposed by Carpinteri (Carpinteri, 1989) for plain concrete beams, and more recently extended by Carpinteri and co-authors (Carpinteri et al., 2009c) to deals also with reinforced concrete elements, is herein adopted. According to such an approach, the concrete beam is modeled as constituted by two parts exhibiting an elastic behavior and connected in correspondence of the mid-span cross-section, where the crack propagation is allowed. The crack propagation is described by the cohesive crack model. All the details of the numerical implementation are given in (Carpinteri et al., 2009c; Carpinteri et al., 2010).

The algorithm permits to track step-by-step the crack propagation and to determine the corresponding resistant load and the mid-span deflection. Starting from the initial configuration (pre-notched concrete beam), the loading process is simulated by imposing a step-by-step crack tip propagation. At each step of calculation, the crack tip is advanced by a fixed amount and the load corresponding to the attainment of the critical condition for crack propagation, i.e. the tensile stress in the fictitious crack tip is equal to the material strength, is sought. In a first stage, only the fictitious crack tip propagates, whereas the real crack tip starts to propagate only when the critical value defined by the cohesive crack law for the crack opening is overcome. The cohesive constitutive laws adopted for the simulations of the three specimens are shown in Figure 3.26. The tensile strength has been assumed equal to 1.7 MPa for the three sizes, whereas the fracture energy has been changed, according to values obtained from the experimental tests. The shape of the cohesive laws has been chosen as bilinear, whereas the values of the critical crack opening,  $w_c$ , and the position of the knee of the constitutive law, point A in Figure 3.26, are varied in order to optimize the fitting with the experimental load-displacement curves. The value of  $w_c$  is 0.13 mm, 0.24 mm and 0.35 mm for specimen B1, B2 and B3, respectively. The values of the crack opening displacement and the stress correspondent to point A are 0.035 mm and 0.55 MPa for specimen B1, 0.064 mm and 0.55 MPa for specimen B2, and 0.077 mm and 0.55 MPa for specimen B3. The load vs. deflection curves obtained from the simulations are compared to the experimental ones in Figure 3.27.

The almost perfect agreement between numerical and experimental results in terms of the global response gives us the confidence that also the cracking

behavior, i.e. the step-by-step crack propagation and the distributions of stresses and displacements along the crack, is close to reality. The evolution of the energy dissipation is therefore calculated on the basis of the numerical results. At each step of crack propagation, the dissipated energy can be precisely computed on the basis of the cohesive constitutive law. As an example, let us consider that at a certain step of calculation, the crack opening in correspondence of a point along the fictitious crack increases from  $w_A$  to  $w_B$  (see Figure 3.26). The corresponding energy per unit area dissipated by this point is therefore represented by the shaded area in the diagram in Figure 3.26. The integration of such contributions over the total fictitious crack area gives the energy dissipated in the considered step. In order to evaluate the rate of the dissipated energy, the mid-span deflection axis has been converted into time, by comparison with the experimental results.

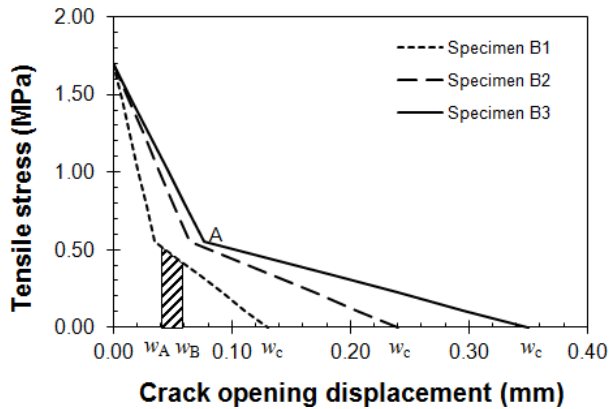


Figure 3.26: Cohesive constitutive laws for the three specimens.

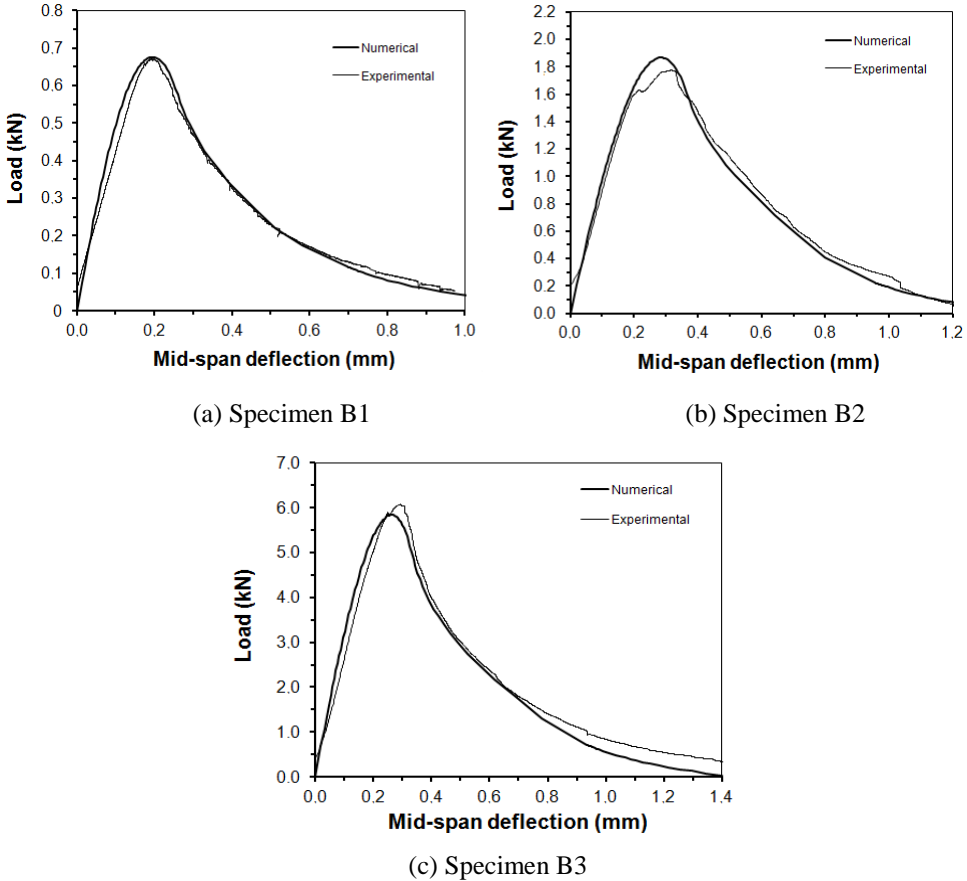
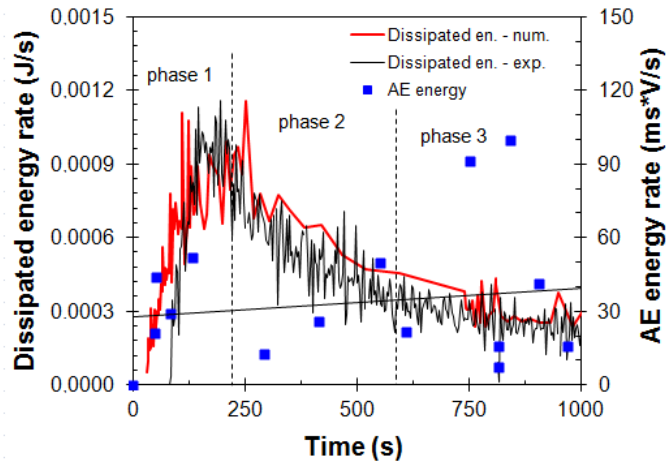


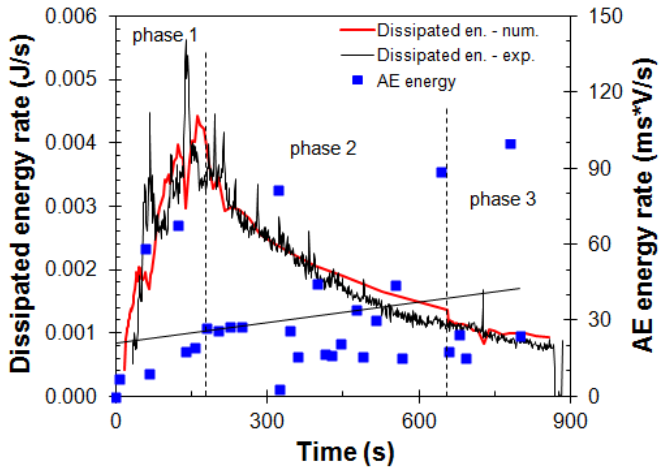
Figure 3.27 (a),(b),(c): Comparison between experimental load vs. displacement curves and corresponding numerical simulations for the three specimens.

The computed energy rates for the three specimens are shown in Figure 3.28, as a function of time. A good agreement has been obtained between experimentally and numerically evaluated dissipated energy rates (thin black and thick red lines, respectively), further confirming the reliability of the numerical

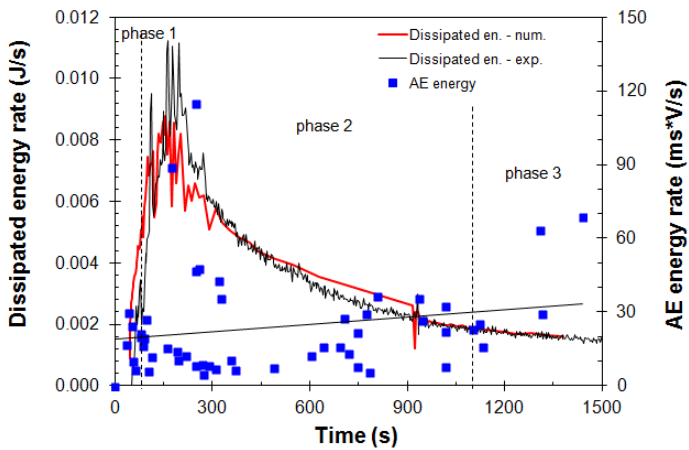
approach. These curves, even if highly irregular, evidence a clear trend for the dissipated energy rate, common to the three tests: it rapidly increases in the first part of the test, when much energy is spent to create and increase the process zone (phase 1), then, it starts to decrease when the second part of the cohesive law (that with a lower slope) comes into play in the process zone (phase 2) and, finally, it continues to decrease when the real crack propagates with a consequent reduction of the process zone up to vanish at the complete failure of the specimen (phase 3). Even though the trend is similar for the three cases, the values of the rate increase by increasing the specimen size. As regards the emitted energy rate, a completely different behavior has been obtained. A strong oscillation of the values is evidenced during all the loading process, with a slight tendency to increase by approaching the end of the test (see the thin straight line in Figure 3.28, representing a linear interpolation of the data). Certainly, their trend is completely uncorrelated to that of the dissipated energy rate. Furthermore, the range of variation of the values is almost independent of the specimen size.



(a) Specimen B1



(b) Specimen B2



(c) Specimen B3

Figure 3.28 (a),(b),(c): Energy dissipation rate and AE energy rate as a function of time for the three specimens.

### 3.2.3 Uniaxial compression tests

Different compression tests were also performed. In particular, cylindrical concrete specimens with diameter equal to 80 mm and length equal to 160 mm were subjected to compression up to the final collapse by means of a servo-hydraulic testing machine.

The specimens were arranged between the press platens without the interposition of friction-reducer layers. Due to the expected brittle response, the tests were conducted by imposing a fixed velocity (0.002 mm/s) to the circumferential expansion. To this aim, the circumferential strain was measured by means of an extensometer attached to a linked chain placed around the cylinders at mid-height (Figure 3.29). This control permits to completely detect the load-displacement curve, even in case of severe unstable phenomena such as snap-back. Due to the limited dimension of the specimens, AE detection was performed by means of a single sensor, applied on the lateral surface of the samples.



Figure 3.29: Experimental set up of the compression test on a cylindrical concrete specimen.

In the following, one of the most relevant tests, is reported.

The load vs. time curve for the compression test is reported in Figure 3.30. In the same figure the AF and RA values of the detected signals, and the cumulated diagram of the AE events are also represented. The compressive strength resulted to be equal to 69.6 MPa.

A dominant presence of Mode I cracks seems to characterize the damage evolution in the first phase of the test, from the beginning up to 1000 s (Figure 3.31a). During a second phase, up to 2500 s, the RA values increase although the prevalent cracking mode is still the opening mode (Figure 3.31b). Finally, from 2500 s up to the end of the test (about 3800 s), a further increase in the RA values is observed. At the same time, a shift from higher to lower frequencies takes place, involving both tensile cracks (low RA) and shear cracks (high RA), as shown in Figure 3.31c.

Therefore, the collapse of the specimen is reached by different modalities of fracture: Mode I splitting failure dominates the mechanical response, whereas a crushing mode, characterized also by friction components (Carpinteri et al. 2007b), appears by approaching the final stage (Figure 3.31d).

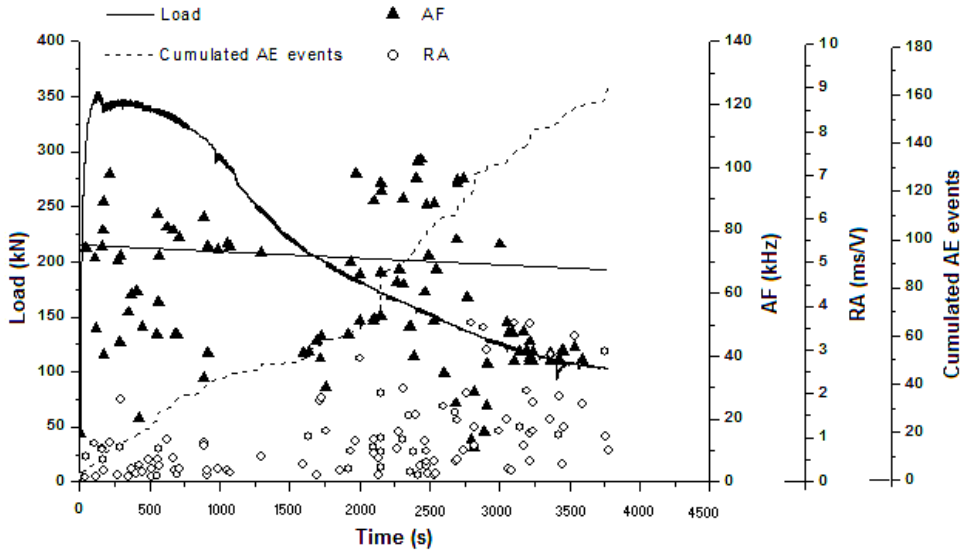
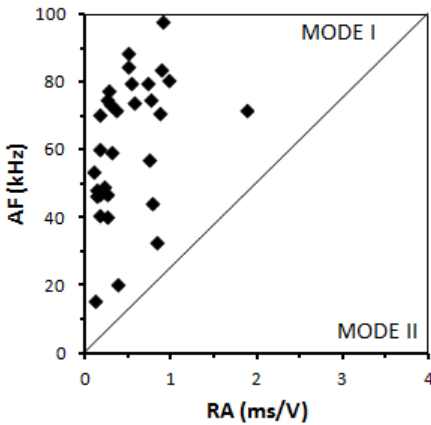
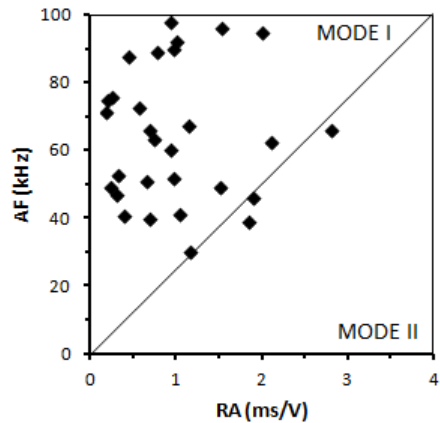


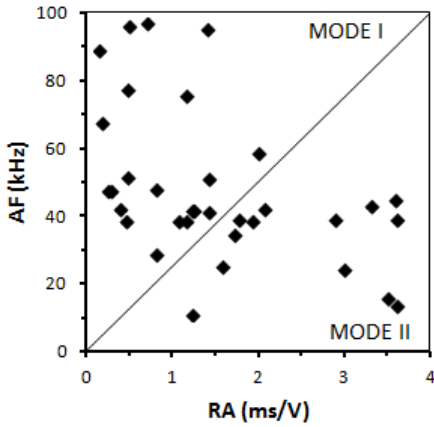
Figure 3.30: Compression test: Load vs. time curve, AF and RA values of the detected AE events, and cumulated diagram of the AE events. The straight line represents the linear regression of the AF values during the test.



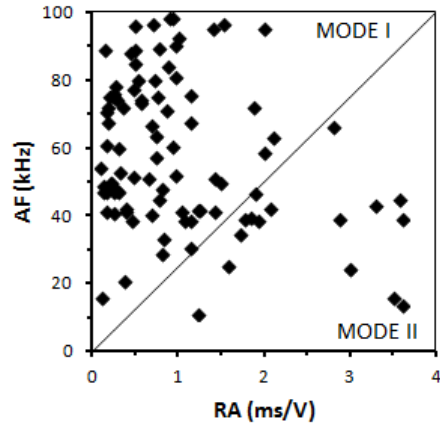
(a)



(b)



(c)



(d)

Figure 3.31: Fracture mode identification by means of the relationship between RA and AF values for a concrete specimen under compression: (a) from 0 to 1000 s; (b) from 1000 s to 2500 s; (c) from 2500 s to the end of the test; (d) total duration of the test.

### 3.3 Conclusions

The present study discusses about the analysis of the AE parameters acquired during experimental tests. In particular, tensile tests, three-point bending tests on notched concrete beams and compression tests on cylindrical specimens were performed. These analyses allowed to identify the source localization, the dominant fracture mode and to investigate on the evolution of the energy release due to damage.

#### 3.3.1 Uniaxial tensile tests

Different re-bars B450C were tested to obtain detailed information about the fracture localization and the type of cracks. During the tensile tests the steel bars were monitored by three AE piezoelectric (PZT) transducers.

- 1) AE sources were determined. In the considered sample, during the elastic phase, the transducers localized AE points in correspondence of both the upper and lower jaw. When the yielding trend started up to the end of the test, a major points concentration was observed between the sensors S2-S3. More in detail, the steel specimen collapsed closer to the sensors S3.
- 2) It was experimentally observed that the wave propagation velocity changed during the different phases of the tensile loading. In addition, for each sensor a shift from higher to lower frequencies was obtained up to the end of the test. Applying the relationship between speed and frequency ( $\lambda = v/f$ ), it was also verified as the wavelength of the AE waves appears

to be of the same order of magnitude of crack size or crack advancement length (about 0.02 m).

- 3) The collapse of the specimen was reached by a Mode I type of fracture, even if friction components between the steel bar and the press jaws characterized the initial stage of the test.

### **3.3.2 Three point bending tests**

The AE parameters were measured by the average values obtained through two sensors positioned at different distances from the notch. From the analyses, the following conclusions may be drawn.

- 1) For all beams a shift from higher to lower frequencies was observed by approaching the final stage of the loading process. Considering also that the RA values are commonly low, a dominance of tensile cracks (Mode I) was found.
- 2) As regards the peak amplitude, a linear decrease proportional to the signals propagation length was obtained. This is due to wave attenuation and distortion that occurs in inhomogeneous media. Obviously these phenomena are reduced on laboratory specimens; whereas they have a greater effect on real structures where the propagation lengths of acoustic waves are longer. The sensors have to cover a larger area, therefore the AE parameters are subjected to a more evident attenuation mechanism. This phenomenon can be studied in the future to obtain correct results as regards the mode of cracking also for large structures.

- 3) The total mechanical dissipated energy and the corresponding values of the fracture energy were calculated for the three beams according to the RILEM Recommendations (RILEM, 1986). A considerable increase in the fracture energy was evidenced by increasing the specimen size. This is a consequence of the well-known scale effects on the toughness in quasi-brittle materials, as explained in (Carpinteri and Chiaia, 1996), and the variation in the maximum aggregate diameter of the concrete mix with the beam size.
- 4) For the three beams, the energy of the AE signals detected during the tests was also evaluated in accordance with the RILEM TC 212-ACD Recommendations (RILEM, 2010a). The AE energy per surface unit decreases by increasing the specimen size, exhibiting, therefore, an opposite trend compared to that of the fracture energy (see Figure 3.22 and Table 3.4). Such a discrepancy suggests that there is no a direct correlation between the two parameters. In fact, the AE energy is an emitted energy, consequent to a surplus of released energy with respect to the dissipated one, that takes place in the case of snap-back instabilities. These instabilities mainly occur when the materials have a macrostructural catastrophic failure, such as the collapse of brittle rock specimens in compression (Carpinteri et al., 2013b). However, local instabilities can develop also at a microscale level during a normal softening behavior, due to the fact that cracks growth in a discontinuous manner (see Figure 3.24). The more pronounced the instabilities are, the higher the emitted energy is. Therefore, it can be concluded that the energy that is globally released during the loading process is partially converted in dissipated energy, that corresponds to the

Griffith energy necessary to create the fracture surfaces, and partially transformed in emitted energy, that can be detected by the AE technique.

- 5) Finally, the differences between dissipated and emitted energy rates were analyzed on the basis of the evolution of these two quantities over the time, during the progress of the experimental test. A numerical simulation of the mechanical response of the TPB tests was performed by the cohesive crack model. Afterwards, the computed experimental and numerical mechanical dissipated energy rates were compared with the AE energy rate detected by each sensor, as a function of time. From this analysis, it was possible to observe that the dissipation energy rate rapidly increases and reaches its maximum value around the peak load. During the softening phase the dissipation rate decreases up to the end of the test. As regards the AE emitted energy rate, the trend slightly increases up to the end of the test. Therefore, this is a further confirmation that the two energies have a different origin.

### **3.3.3 Uniaxial compression tests**

Different compression tests were performed on cylindrical concrete specimens with diameter equal to 80 mm and slenderness  $\lambda=2$ .

In the considered sample, the collapse was reached by different modalities of fracture. Mode I splitting failure dominates the initial mechanical response, whereas a crushing mode, characterized also by friction components (Mode II), appears by approaching the final stage.

## **4 Case Study: In-situ Monitoring at the San Pietro-Prato Nuovo Gypsum Quarry located in Murisengo (Alessandria), Italy**

### **4.1 Introduction: The San Pietro-Prato Nuovo Gypsum Quarry**

The San Pietro - Prato Nuovo quarry in Murisengo, is currently structured in five levels of underground development and from which high quality gypsum is extracted every day.

Gypsum is a soft sulfate mineral composed of calcium sulfate dihydrate, with the chemical formula  $\text{CaSO}_4 \cdot 2\text{H}_2\text{O}$ . It can be used as a fertilizer, is the main constituent in many forms of plaster and is widely mined.

The structural stability in each level is assured by an archway-pillar system (Figure 4.1) which unloads over the underlying floor of average thickness of 4 m. Through accurate topographic surveys, it was possible to ensure a good coaxiality of the pillars between the different levels. In this way dangerous loads eccentricity were avoided.



Figure 4.1: the San Pietro - Prato Nuovo gypsum quarry.

## 4.2 The structural monitoring

Monitoring and detection of the different forms of energy emitted during the failure of natural and artificial brittle materials allow an accurate interpretation of damage in the field of Fracture Mechanics. These phenomena have been mainly measured based on the signals captured by the acoustic emission (AE) measurement systems (Carpinteri et al., 2006c; Carpinteri et al., 2006d; Carpinteri et al., 2007a; Carpinteri et al., 2009b; Carpinteri et al., 2009d; Carpinteri et al., 2009e; Lockner et al., 1992; Mogi, 1962; Ohtsu, 1996; Shcherbakov and Turcotte, 2003). Nowadays, the AE technique is well-known in the scientific community and applied for monitoring purpose. In addition, based on the analogy between AE and seismic activity, AE associated with microcracks are monitored and power-law frequency vs. magnitude statistics are observed.

Preliminary results, acquired at a gypsum mine situated in the Northern Italy (Murisengo, AL) and related to the evaluation of acoustic phenomena are reported. The monitoring system is based on the simultaneous acquisition of the Acoustic and Neutron emissions detection, even if in this work, only the AE monitoring will be considered.

Anyway, this method allows to control the structural stability of the mine carrying out, at the same time, the environment monitoring for the seismic risk evaluation.

Taking into account the relationship between AE, NE and seismic activity it will be possible to set up a sort of alarm systems that could be at the base of a warning network. This warning system could combine the signals from other alarm stations to prevent the effects of seismic events and to identify the earthquakes' epicentres.

#### **4.2.1 AET and NET Monitoring Setup**

Preliminary laboratory compression tests on gypsum specimens with different slenderness were conducted. The AE activity emerging from the compressed specimens was detected by a piezoelectric (PZT) transducer glued on the external surface, resonant at 78 kHz, which is able to convert the high-frequency surface motions due to the acoustic wave into electric signals (the AE signal). Resonant sensors are more sensitive than broadband sensors, which are characterized by a flat frequency response in their working range, and then they can be successfully used in monitoring of large-sized structures (Carpinteri et al., 2006c; Carpinteri et al., 2007a).

For an accurate neutron evaluation, a  $^3\text{He}$  radiation monitor was used. During the experimental trial the neutron field monitoring was carried out in “continuous mode”. The AT1117M (ATOMTEX, Minsk, Republic of Belarus) neutron device is a multifunctional portable instrument. This type of device provides a high sensitivity and wide measuring ranges (neutron energy range 0.025 eV–14 MeV), with a fast response to radiation field change ideal for environmental monitoring purpose.

#### 4.2.2 Experimental tests

Preliminary laboratory compression tests on gypsum specimens were conducted in view to a permanent installation for *in-situ* monitoring.

Different gypsum samples with a diameter  $D = 75$  mm and different slenderness ( $\lambda = 0.5$ ,  $\lambda = 1$  and  $\lambda = 2$ ), taken from Murisengo mine, were used. For these tests a standard servo-hydraulic press with a maximum capacity of 1000 kN, equipped with control electronics, was employed. This machine makes it possible to carry out tests in either load or displacement control. The tests were performed in piston travel displacement control by setting, for all the tested specimens, a velocity of 0.001 mm/s during compression.

The AE signals were detected by applying to the sample surface the piezoelectric transducer described above (Figure 4.2).



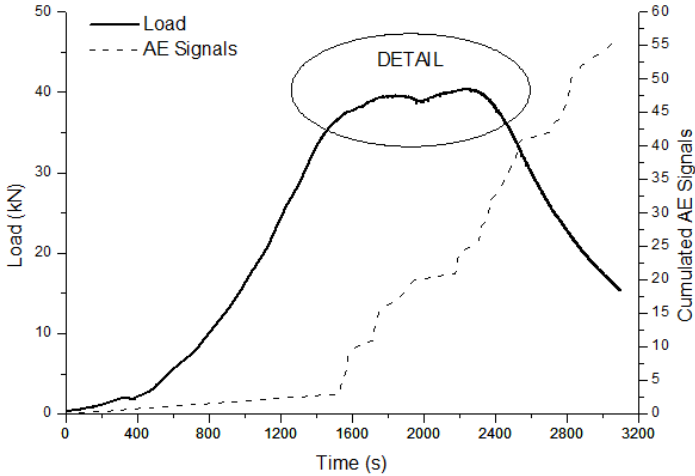
Figure 4.2: AE piezoelectric transducer positioned around the monitored gypsum specimen.

In the following, three of the most relevant samples are reported. In more detail, in Figure 4.3a, the load vs. time diagram compared with the cumulated AE signals for the gypsum specimen (S3) with slenderness  $\lambda = 2$  are represented. Similar results were obtained for the other two elements.

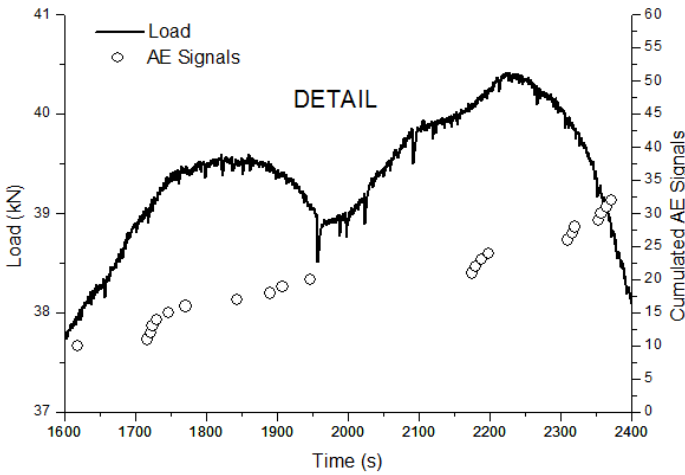
The considered sample, that is characterized by an evident ductile behaviour, reached a maximum load of about 40 kN. In particular, starting from the first peak load, a significant increase in the cumulated AE is observed. The AE signals achieved the maximum rate in proximity of the peak loads, while in the post peak phase, during the softening trend, the AE rate diminished.

Moreover, as shown in detail in Figure 4.3b, it is observed that gypsum is characterized by weak and frequent stress drops, around which AE signals have accumulated. This AE distribution reinforces the idea that in this particular phases

the accumulated energy is suddenly released, due to micro-cracks formation (Carpinteri and Massabò, 1997; Carpinteri and Monetto, 1999).



(a)



(b)

Figure 4.3: (a) load vs. time curve and cumulated diagram of the AE events. (b) Detail of load vs. time curve, and AE cumulated number in the vicinity of the peaks load.

### **4.2.3 In-situ monitoring**

From April 1st, 2014 a dedicated in-situ monitoring at the San Pietro - PratoNuovo gypsum quarry located in Murisengo (AL), Italy is started and it is still in progress. More in detail, a pillar of 8x8x6 m situated on the fifth floor (about 100 meters below the ground level), was monitored.

A hole of about 4x4 m has been made on the pillar (see the red square in Figure 4.4a). In this way, the detensioned surface layer with a thickness of about 50 cm, was removed. Therefore, the monitoring was carried out directly on the resistant pillar section, which was not disturbed by the rock blasting.

Currently the quarry is subjected to a multiparameter monitoring, by the AE technique and the detection of the environmental neutron field fluctuations, in order to assess the structural stability and, at the same time, to evaluate the seismic risk of the surrounding area. The dedicated "USAM" AE acquisition system consists of 6 PZT transducers (Figure 4.4b,c), calibrated over a wide range of frequency comprised between 50 kHz and 800 kHz, 6 units of data storage provided of triggers and a central unit for the data synchronization.

The AE signals received by all the transducers are analysed by means of a threshold detection device that counts the signal bursts exceeding a certain electric tension (measured in volts (V)). Throughout the monitoring period, the threshold level for the detection of the input signals coming from the PZT transducers was kept at 100 mV. In fact, this level is the most significant for the detection of AE signals from damage processes in non-metallic materials.

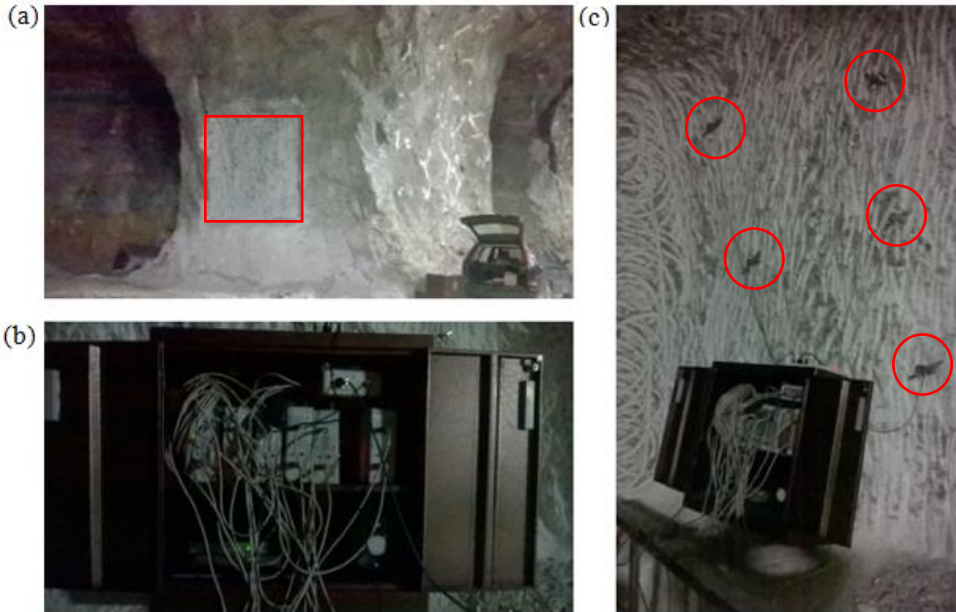


Figure 4.4: (a): hole 4x4 m without detensioned surface layer; (b,c) AE Monitoring set.

A plot of the cumulative AE count obtained on the basis of the number of events detected per monitoring day is shown in Figure 4.5. The curve was plotted starting from the date of application of the sensors to May 19, 2014.

From Figure 4.5 it is possible to observe that the plot of the cumulative AE count has a quasi-linear trend. Only few frequency and amplitude increments can be observed.

However, the small discontinuities in the cumulative AE count curve denote the critical moments during which the release of energy from the microcrack formation process is greatest. Moreover, the  $b$ -value estimation indicates also that the monitored pillar is actually undergoing to a damage process (Carpinteri et al., 2009b; Carpinteri et al., 2009d; Carpinteri et al., 2009e). As a matter of fact high

$b$ -values is linked to diffused microcracking, while, to the other hand, low  $b$ -values correspond to macrocrack growth.

The  $b$ -value (near to 1.5) indicates that the pillar is subjected to a diffused microcracking. But, during the monitored period, a minimum value near to 1 is observed to which corresponds a cluster of cracks forming closed to a preferential fracture surface.

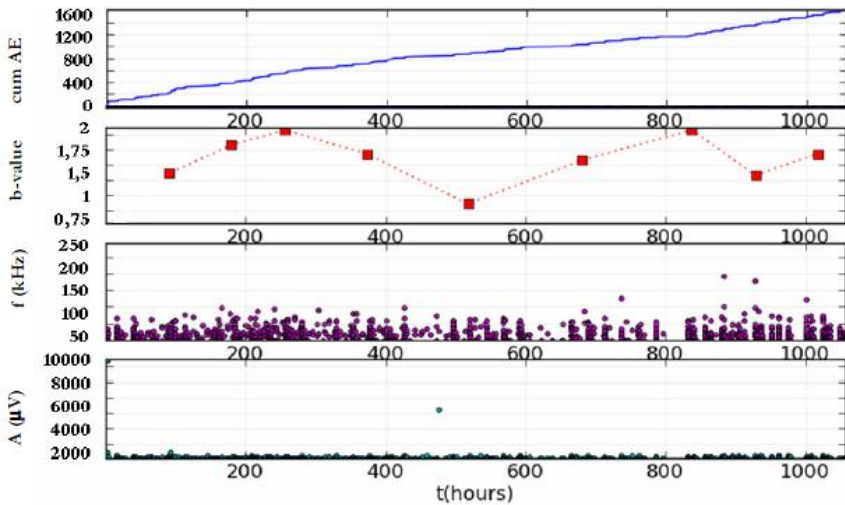


Figure 4.5: Cumulated AE activity,  $b$ -value, AE frequency and AE amplitude relating to the pillar monitored during the experimental campaign.

Moreover, a comparison between the earthquakes (ISIDE Working Group, 2010) occurred in the immediate vicinity of the monitored area during the experimental campaign was carried out. The AE count rate distribution in terms of events/hour compared to the usual seismic activity of the area (red stars) –recorded within a 100-km radius from the quarry site–is shown in Figure 4.6. The experimental observation reveals a correlation between the AE events and the

most intense and closed seismic events (ISIDe Working Group, 2010). As can be seen evident peaks in acoustic emission were detected in the monitored period. In particular, the highest AE count peak (ca 60) was detected on April 2, 2014 when the surrounding area was hit by some quakes, the most intense of them of magnitude 4.8. Therefore, the most significant acoustic emission increments happened before or after quakes occurrence.

This further experimental evidence strengthens the idea that acoustic emissions –and also considering gas radon emission that appears to be one of the most reliable seismic precursors– it will be possible to set up a sort of monitoring systems that could perform a warning environmental monitoring.

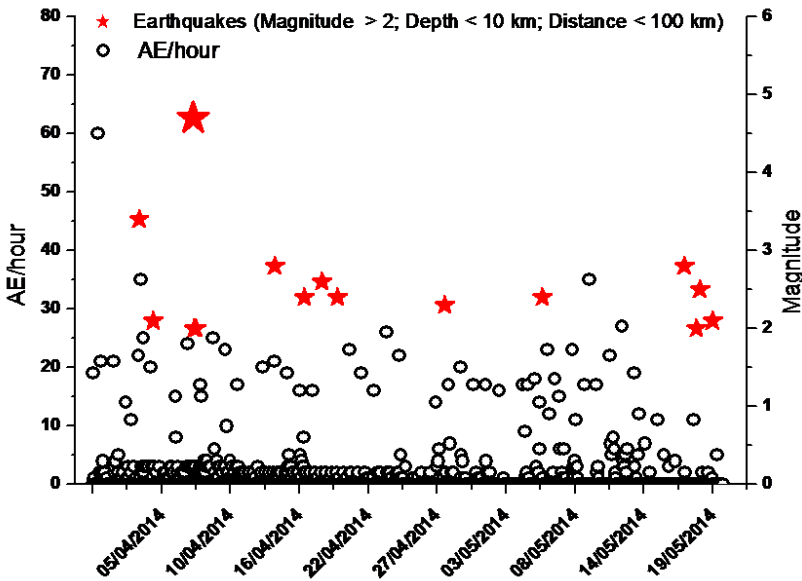


Figure 4.6: AE rate compared to local seismic activity.

### 4.2.3.1 AE source localization

An accurate localization of the AE sources on the monitored pillar was obtained using the USAM AE acquisition system composed of 6 PZT transducers, which had permitted to measure the arrival times of each AE signals.

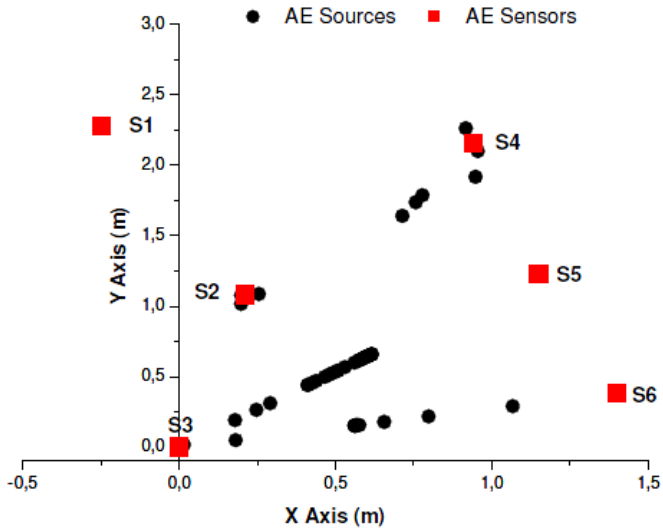
Applying the source location methods described in section 1.2.4, the AE sources are determined. Considering that the six sensors are positioned on a plane, so their z-coordinates are the same, the cracks location is distributed along the x and y axes. The origin of the reference system Oxyz is the lower left sensor S3.

In Table 4.1, the coordinates of the sensors are summarized.

SENSOR	X (m)	Y (m)	Z (m)
S1	-0.25	2.28	0
S2	0.21	1.08	0
S3	0	0	0
S4	0.94	2.16	0
S5	1.15	1.23	0
S6	1.40	0.38	0

Table 4.1: x, y and z coordinates of the six sensors.

From Figure 4.7a, it is possible to evaluate the main propagation directions of the microcracking during the monitoring. The AE sources are depicted with black points. In particular, many AE localized points are concentrated between the sensor S2-S4, S3-S5 and S3- S6. Therefore, three preferential crack propagation paths can be observed (Figure 4.7b).



(a)



(b)

Figure 4.7: (a) AE source localization (b) preferential crack propagation.

### 4.3 Damage evaluation of the monitored pillar by AE

The AE technique is able to analyze state variations in a certain physical system and can be used as a tool for predicting the occurrence of “catastrophic” events. In many physics problems (for example when studying test specimen failure in a laboratory, the modalities of collapse of a civil structure, or the localization of the epicentral volume of an earthquake), the modalities of a collapsed structure are generally analyzed “after” the event. This technique can be used, instead, to identify the premonitory signals that “precede” a catastrophic event, as, in most cases, these warning signs can be captured well in advance (Kapiris et al., 2004; Rundle et al., 2003; Shcherbakov and Turcotte, 2003; Zapperi et al., 1997).

#### 4.3.1 A fractal criterion for AE monitoring

Fragmentation theories have shown that during microcrack propagation, energy dissipation occurs in a fractal domain comprised between a surface and the specimen volume,  $V$  (Carpinteri and Pugno, 2002; Carpinteri et al., 2004). On the other hand, during microcrack propagation, acoustic emission counts can be clearly detected. Since the energy dissipated,  $E$ , is proportional to the number of AE counts,  $N$ , the critical density of acoustic emission counts,  $\Gamma_{AE}$ , can be considered as a size-independent parameter:

$$\Gamma_{AE} = \frac{N_{max}}{V^{D/3}} \quad (4.1)$$

where  $\Gamma_{AE}$  is the fractal acoustic emission density, and  $N_{max}$  is the total number of counts evaluated at peak-stress,  $\sigma_u$ , when the critical condition is reached.  $D$  is the so-called fractal exponent, comprised between 2 and 3. Eq. (4.1) predicts a volume-effect on the maximum number of AE counts for a specimen tested to failure (Carpinteri et al., 2007a).

The extent of structural damage can be worked out from the AE data recorded on a reference specimen (subscript  $r$ ) obtained from the structure and tested to failure. Naturally, the fundamental assumption is that the damage level observed in the reference specimen is proportional to the level reached in the entire structure before monitoring is started.

From Eq. (4.1) we get:

$$N_{max} = N_{maxr} \left( \frac{V}{V_r} \right)^{D/3} \quad (4.2)$$

from which we can obtain the critical number of AE counts,  $N_{max}$ , for the structure.

The time dependence of the structural damage observed during the monitoring period can also be correlated to the rate of propagation of the microcracks.

If we express the ratio between the cumulative number of AE counts recorded during the monitoring process,  $N$ , and the number obtained at the end of the observation period,  $N_d$ , as a function of time,  $t$ , we get the damage time dependence on AE:

$$\frac{N}{N_d} = \left( \frac{t}{t_d} \right)^{\beta_t} \quad (4.3)$$

where  $t_d$  parameter is residual life-time of the structure. By working out the  $\beta_t$  exponent from the data obtained during the observation period, we can make a prediction as to the structure's stability conditions. If  $\beta_t < 1$ , the damaging process slows down and the structure evolves towards stability conditions, in as much as

energy dissipation tends to decrease; if  $\beta_t > 1$  the process becomes unstable, and if  $\beta_t = 1$  the process is metastable, i.e., though it evolves linearly over time, it can reach indifferently either stability or instability conditions (Carpinteri and Lacidogna, 2006a).

### 4.3.2 Critical behavior interpreted by AE

In order to assess the extent of damage in the zone monitored using the AE technique, different compressive tests were conducted on some gypsum specimens characterized by three different slenderness ( $\lambda=0.5$ ;  $\lambda=1$  and  $\lambda=2$ ).

Three samples were chosen. The results obtained for the biggest element ( $\lambda=2$ ), is shown in Figure 4.3. From this diagram, it is possible to observe that the cumulative number of AE counts at failure stress (i.e. before the critical condition is reached) is  $N_{\max} = 24$ . The experimental results obtained on the three considered gypsum elements are summarized in Table 4.2.

Specimen	Volume (cm <sup>3</sup> )	Peak Stress (MPa)	$N_{\max}$ at $\sigma_u$
1 ( $\lambda=0.5$ )	166	20.87	8
2 ( $\lambda=1$ )	331	16.61	15
3 ( $\lambda=2$ )	663	9.15	24

Table 4.2: Experimental values obtained from compression tests and AE measurements.

As can be seen from Table 4.2, in compressive tests the peak stress in the gypsum specimen is a decreasing function of the slenderness ratio, whereas the cumulative number of AE counts increases with increasing specimen volume. The

specimen slenderness has significant effects on peak stresses  $\sigma_u$ , and size effects are highly significant on the critical number of acoustic emission  $N_{max}$ .

Peak stress, in fact, can be correlated to the quantity of defects present in the material, therefore the damaged volume is proportional to the released energy measured by the AE technique.

From a statistical analysis of the experimental data, parameters  $D$  and  $\Gamma_{AE}$  (Eq. 4.1)) can be quantified. Parameter  $D$  represents the slope, in the bilogarithmic diagram, of the curve correlating  $N_{max}$  to the specimen volume. By bestfitting, we obtain  $D/3 = 0.792$  (Figure 4.8), so that the fractal exponent, as predicted by fragmentation theories, turns out to be between 2 and 3 ( $D = 2.38$ ). Moreover, the critical value of fractal AE density turns out to be  $\Gamma_{AE} \cong 7.00 \text{ cm}^{-2.38}$ .

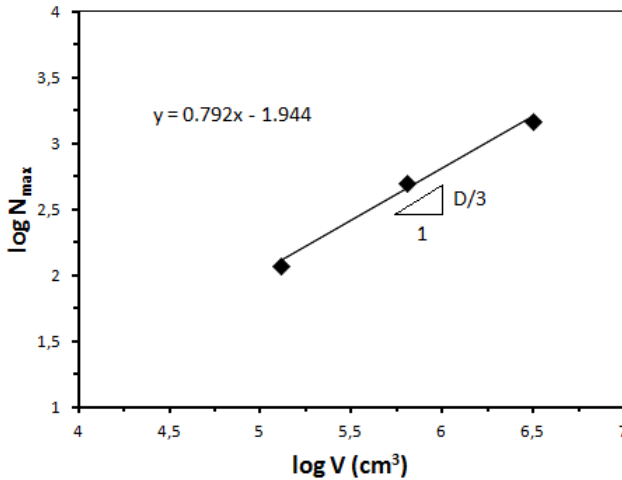


Figure 4.8: Volume effect on  $N_{max}$ .

In general, the effects of slenderness on parameter  $N_{max}$  is proportional to the area subtended by the stress–strain curve.

This area is correlated to the ductility of the material, which, as a rule, is not proportional to its strength. For these reasons, when monitoring full scale structures, it is reasonable to make predictions on the maximum number of AEs that would lead to the critical stage, by taking into account the total volume damaged.

### 4.3.3 Damage level of the monitored pillar

During the first observation period, which lasted 48 days, the number  $N$  of AE counts recorded was 1606 (see Figure 4.5). The gypsum pillars at the fifth floor have a base area of about  $800 \times 800 \text{ cm}^2$ ; while the average height is about 600 cm. Therefore the total volume of the monitored pillar will be  $V \cong 800 \times 800 \times 600 \text{ cm}^3 = 38.4 \times 10^7 \text{ cm}^3$ . From Eq. (4.2), using fractal exponent  $D = 2.38$ , we obtain a critical AE number of  $N_{\max} \cong 8.86 \times 10^5$ .

In order to obtain indications on the rate growth of the damage process in the pillar, as given in Eq. (4.3), the data obtained with the AE technique were subjected to best-fitting in the bilogarithmic plane. Figure 4.9 shows that the slope  $\beta_t$  is equal to 0.720. This means that the structure evolves towards stability conditions ( $\beta_t < 1$ ).

Introducing the values of  $N_{\max}$  into Eq. (4.3), the value  $t$  obtained is  $67.8 \times 10^5$  hours. The remaining life-time of this structure is therefore defined, in terms of time before the maximum number of AE counts is reached in the analyzed zone, at about 774 years.

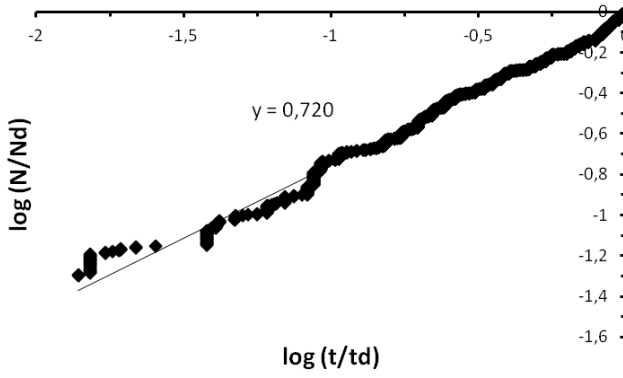


Figure 4.9: Evolution of damage.

## 4.4 Conclusions

From April 1st, 2014 a dedicated in-situ monitoring at the San Pietro - Prato Nuovo gypsum quarry located in Murisengo (AL) - Italy, is started and it is still in progress. More in detail, a pillar of 8x8x6 m situated on the fifth floor (about 100 meters below the ground level), has been monitored.

### 4.4.1 Experimental compression tests

Preliminary laboratory compression tests on gypsum specimens were conducted with the AE technique. In more detail, gypsum samples with a diameter  $D = 75$  mm and different slenderness ( $\lambda = 0.5$ ,  $\lambda = 1$ , and  $\lambda = 2$ ), taken from Murisengo mine, were used.

It was observed that the material is characterized by a ductile behaviour and by frequent stress drops, around which AE signals were accumulated. This AE distribution reinforces the idea that in these particular phases the emitted energy is suddenly released, due to micro-cracks formation (Carpinteri and Massabò, 1997; Carpinteri and Monetto, 1999).

### 4.4.2 *In-situ* monitoring

As regards the *in-situ* monitoring, preliminary results related to the evaluation of acoustic phenomena, are reported.

- 1) The b-value estimation (near to 1.5) indicates that the pillar is subjected to a diffused microcracking. But a minimum value near to 1 was also observed, to which corresponds a cluster of cracks forming closed to a preferential fracture surface (Carpinteri et al., 2009b; Carpinteri et al., 2009d; Carpinteri et al., 2009e).
- 2) AE sources were localized: in particular, the AE points are concentrated along three preferential crack propagation paths.
- 3) The experimental data obtained emphasize the close correlation between acoustic emissions and seismic activity. From the monitoring it is possible to observe that the most significant acoustic emission increments happened before or after quakes occurrence. Therefore, by integrating all these signals, it will be possible to set up a sort of alarm systems for the prediction and diagnosis of earthquakes. These sensors could be applied at certain depths in the soil, along the most important faults, or very close to the most seismic areas to prevent well in advance the effects of seismic events and to identify the epicentre of an earthquake.

#### **4.4.3 Damage evaluation by AE**

A sound safety assessment should take into account the evolution and the interaction of different damage phenomena. In this connection, AE monitoring can be highly effective. This technique makes it possible to introduce an energy based damage parameter for structural assessment which establishes a correlation between AE activity in a structure and the corresponding activity recorded on specimens taken from the structure and tested to failure.

From the analyses, the following conclusions may be drawn.

- 1) In order to obtain indications on the growth rate of the damage process in the pillar, the parameter  $\beta_t$  was calculated. Considering that  $\beta_t = 0.720$ , therefore less than 1, the structure evolves towards stability conditions (Carpinteri and Lacidogna, 2006a).
- 2) In conclusion, the remaining life-time of this structure was defined, in terms of time before the maximum number of AE counts is reached in the analyzed zone, at about 774 years.



## **5 Conclusions**

Structural Health Monitoring (SHM) allows to provide accurate information concerning the physical conditions and performance of structures. Its purpose is to detect the structural behavior in quasi-real-time, indicate the approximate position of problems on the structure and determine their importance. An advanced method of quantitative non-destructive evaluation of damage progression is represented by the Acoustic Emission (AE) Technique.

### **5.1 Experimental tests**

In this research, the Acoustic Emission monitoring was used to evaluate the fracture propagation process during tensile tests, three-point bending (TPB) tests on notched concrete beams, and compression tests. The most representative AE parameters were measured by sensors in order to obtain detailed information on the signals attenuation and localization as well as on the type of cracks. The waves frequency and the Rise Angle allowed to discriminate the prevailing cracking mode from pure opening or sliding; while the cumulated number of AE events and their amplitude were used to compute the signal energy.

In *tensile tests* the AE sources were localized, considering that the relative arrival times of the acoustic signals to each transducer and the positions of the three sensors were known.

Furthermore, it was experimentally observed that the wave propagation velocity changed during the different phases of the tensile loading. In addition, for each sensor a shift from higher to lower frequencies was obtained up to the end of the test. Applying the relationship between speed and frequency ( $\lambda = v/f$ ), it was also verified as the wavelength of the AE waves appears to be of the same order of magnitude of crack size or crack advancement length.

*Three-point bending tests* on concrete beams were carried out to evaluate the Acoustic Emission (AE) parameters. A numerical simulation of the mechanical response of the TPB tests was also performed on the basis of the cohesive crack model. Then, the experimental and numerical mechanical energy dissipated to create the fracture surfaces and the energy emitted and detected by the AE sensors were computed and compared on the basis of their cumulative value at the end of the test and their rates during the loading process.

It can be inferred that there is no a direct correlation between the two parameters. This phenomenon occurs because the AE energy is an emitted energy, consequent to a surplus of released energy with respect to the dissipated one. The AE energy emission takes place in the case of macrostructural catastrophic failures, such as the collapse of a brittle rock specimen in compression with snap-back instability (Carpinteri et al., 2013b). However, local instabilities can develop also at a microscale level during a normal softening behavior, due to the fact that cracks growth in a discontinuous manner.

Therefore, the two energies have found to be uncorrelated, although an indirect relationship is given by the fact that their sum corresponds to the total energy released during the test.

Finally, *compression tests* on cylindrical specimens, characterized by slenderness  $\lambda=2$ , were conducted in order to reinforce the effectiveness of the fracture mode identification criteria by means of AE parameters analysis.

## **5.2 In-situ Monitoring at the Gypsum Quarry (Murisengo, Italy)**

A dedicated in-situ monitoring at the San Pietro - Prato Nuovo gypsum quarry located in Murisengo (AL) - Italy, is started and it is still in progress, developing the application aspects of the AE technique.

Preliminary laboratory compression tests on gypsum specimens with different slenderness ( $\lambda=0.5$ ;  $\lambda=1$  and  $\lambda=2$ ) were conducted with the AE technique to assess the validity and efficiency of the system in view to the permanent installation for *in-situ* monitoring.

Currently the quarry is subjected to a multiparameter monitoring, by the AE technique and the detection of the environmental neutron field fluctuations, in order to assess the structural stability and, at the same time, to evaluate the seismic risk of the surrounding area.

A comparison between the earthquakes (ISIDE Working Group, 2010) occurred in the immediate vicinity of the monitored area during the experimental campaign

was carried out. It was observed that the most significant acoustic emission increments happened before or after quakes occurrence.

Therefore, by integrating all these signals - and also considering gas radon emission that appears to be one of the most reliable seismic precursors -, it will be possible to set up a sort of alarm systems that combine AE and neutron sensors for the prediction and diagnosis of earthquakes. These sensors could be applied at certain depths in the soil, along the most important faults, or very close to the most seismic areas to prevent well in advance the effects of seismic events and to identify the epicentre of an earthquake.

Furthermore, AE monitoring proved to be highly effective in the evolution and interaction of different damage phenomena assessment. As a matter of fact, this technique makes it possible to introduce an energy based damage parameter for structural assessment which establishes a correlation between AE activity in a structure and the corresponding activity recorded on specimens taken from the structure and tested to failure.

In this contest, the  $\beta_t$  parameter was calculated in order to obtain indications on the growth rate of the damage process in the monitored pillar. In addition, the remaining life-time of the structure was defined, in terms of time before the maximum number of AE counts will be reached in the analyzed zone.

## References

- Aggelis, D.G., "Classification of cracking mode in concrete by Acoustic Emission parameters". *Mech. Res. Communications*, **38**:153-7 (2011).
- Aggelis, D.G., Shiotani, T., Papacharalampopoulos, A., and Polyzos, D., "The influence of propagation path on acoustic emission monitoring of concrete", *Structural Health Monitoring*, **11**:359-66 (2012a).
- Aggelis, D.G., Mpalaskas A.C., Ntalakas D., and Matikas T.E., "Effect of wave distortion on acoustic emission characterization of cementitious materials". *Construction and Building Materials*, **35**:183-90 (2012b).
- Aldahdooh, M.A.A., and Muhamad Bunnori, N., "Crack classification in reinforced concrete beams with varying thicknesses by mean of acoustic emission signal features". *Constr. Build. Mater.*, **45**:282-8 (2013).
- Brindley, B.J., Holt, J., and Palmer, I.G., "Acoustic Emission-3: the use of ringdown counting", *Non-Destructive Testing*, **6**:299-306 (1973).
- Bruneau, M., and Potel, C., *Materials and Acoustics Handbook*, Wiley, (2009).
- Carpinteri, A., "Interpretation of the Griffith Instability as a Bifurcation of the Global Equilibrium," *Application of Fracture Mechanics to Cementitious Composites*, S.P. Shah, ed., Martinus Nijhoff Publishers, Dordrecht, 287-316 (1985).
- Carpinteri, A., "Mechanical Damage and Crack Growth in Concrete: Plastic Collapse to Brittle Fracture", Martinus Nijhoff Publishers, Dordrecht, 1986.

Carpinteri, A., "Size effects on strength, toughness, and ductility", *Journal of Engineering Mechanics*, **115**:1375-92 (1989).

Carpinteri, A., "Scaling laws and renormalization groups for strength and toughness of disordered materials", *International Journal of Solids and Structures*, **31**:291-302 (1994).

Carpinteri, A., and Chiaia, B., "Size effects on concrete fracture energy: dimensional transition from order to disorder". *Mater. Struct.*, **29**:259-66 (1996).

Carpinteri, A., and Massabò, R., "Continuous vs discontinuous bridged-crack model for fiber-reinforced materials in flexure". *Int. J. Solids. Struct.*, **34**:2321-38 (1997).

Carpinteri, A., and Ferro, G., "Scaling behavior and dual renormalization of experimental tensile softening responses". *Mater. Struct.*, **31**:303-9 (1998).

Carpinteri, A., and Monetto, I., "Snap-back analysis of fracture evolution in multi-cracked solids using boundary element method". *Int. J. Fract.*, **98**:225-41 (1999).

Carpinteri, A., and Pugno, N., "Fractal fragmentation theory for shape effects of quasi-brittle materials in compression", *Magazine of Concrete Research*, **54**:473-80 (2002).

Carpinteri, A., and Lacidogna, G., "Damage diagnosis in concrete and masonry structures by acoustic emission technique", *Journal Facta Universitatis, Series: Mechanics, Automatic Control and Robotics 3*, **13**:755-64 (2003).

Carpinteri, A., Lacidogna, G., and Pugno, N., "Scaling of energy dissipation in crushing and fragmentation: A fractal and statistical analysis based on particle size distribution". *International Journal of Fracture*, **129**:131-39 (2004).

Carpinteri, A., Lacidogna, G., and Pugno, N., "Time-scale effects on acoustic emission due to elastic waves propagation in monitored cracking structures", *Physical Mesomechanics*, **8**:77-80 (2005).

- Carpinteri, A., and Lacidogna, G., "Structural monitoring and integrity assessment of medieval towers", *ASCE Journal of Structural Engineering*, **132**:1681-90 (2006a).
- Carpinteri, A., and Lacidogna, G., "Damage monitoring of an historical masonry building by the acoustic emission technique", *Materials and Structures*, **39**:161-7 (2006b).
- Carpinteri, A., Lacidogna, G., and Niccolini, G., "Critical behaviour in concrete structures and damage localization by acoustic emission", *Key Engineering Materials*, **312**:305-10 (2006c).
- Carpinteri, A., Lacidogna, G., and Pugno, N., "Richter's laws at the laboratory scale interpreted by acoustic emission", *Magazine of Concrete Research*, **58**:619-25 (2006d).
- Carpinteri, A., Lacidogna, G., and Pugno N., "Structural damage and life-time assessment by Acoustic Emission monitoring", *Engineering Fracture Mechanics*, **74**:273-89 (2007a).
- Carpinteri, A., Lacidogna, G., and Niccolini, G., "Acoustic Emission monitoring of medieval towers considered as sensitive earthquake receptors", *Natural Hazards and Earth System Sciences*, **1**:1-11 (2007b).
- Carpinteri, A., Lacidogna, G., Niccolini, G., and Puzzi, S., "Critical defect size distributions in concrete structures detected by the acoustic emission technique", *Meccanica*, **43**:349-63 (2008a).
- Carpinteri, A., Lacidogna, G., and Puzzi, S., "Prediction of cracking evolution in full scale structures by the b-value analysis and Yule statistics", *Physical Mesomechanics*, **11**:260-71 (2008b).
- Carpinteri, A., Corrado, M., Mancini, G., and Paggi, M., "The overlapping crack model for uniaxial and eccentric concrete compression tests", *Magazine of Concrete Research*, **61**:745-57 (2009a).
- Carpinteri, A., Lacidogna, G., and Puzzi, S., "From criticality to final collapse: evolution of the *b*-value from 1.5 to 1.0". *Chaos, Solitons and Fractals*, **41**: 843-53 (2009b).

Carpinteri, A., Corrado, M., Mancini, G., and Paggi, M., "Size-scale effects on plastic rotational capacity of reinforced concrete beams", *ACI Structural Journal*, **106**:887-96 (2009c).

Carpinteri, A., Lacidogna, G., and Niccolini, G., "Fractal analysis of damage detected in concrete structural elements under loading". *Chaos, Solitons and Fractals*, **42**: 2047-56 (2009d).

Carpinteri, A., Lacidogna, G., Niccolini, G., and Puzzi, S., "Morphological fractal dimension versus power-law exponent in the scaling of damaged media". *Int. J. of Damage Mechanics*, **18**: 259-82 (2009e).

Carpinteri, A., Corrado, M., and Paggi, M., "An integrated cohesive/overlapping crack model for the analysis of flexural cracking and crushing in RC beams", *International Journal of Fracture*, **161**:161-73 (2010).

Carpinteri, A., Corrado, M., and Paggi, M., "An analytical model based on strain localization for the study of size-scale and slenderness effects in uniaxial compression tests", *Strain*, **47**:351-62 (2011).

Carpinteri, A., Corrado, M., and Lacidogna, G., "Three different approaches for damage domain characterization in disordered materials: Fractal energy density,  $b$ -value statistics, renormalization group theory", *Mechanics of Materials*, **53**:15-28 (2012).

Carpinteri, A., Lacidogna, G., Manuello A., and Niccolini G., "Acoustic emission wireless transmission system for structural and infrastructural networks". *Proc. VIII International Conference on Fracture Mechanics of Concrete and Concrete Structures FraMCoS-8*, J.G.M. Van Mier, G. Ruiz, C. Andrade, R.C. Yu and X.X. Zhang (Eds), March 10-14, 2013, Toledo, Spain (2013a).

Carpinteri, A., Corrado, M., and Lacidogna, G., "Heterogeneous materials in compression: Correlations between absorbed, released and acoustic emission energies". *Engineering Failure Analysis*, **33**:236-50 (2013b).

- Carpinteri, A., Lacidogna, G., Accornero, F., Mpalaskas, A.C., Matikas, T.E., and Aggelis, D.G., "Influence of damage in the acoustic emission parameters", *Cement & Concrete Composites*, **44**:9-16 (2013c).
- Colombo, S., Main, I.G., and Forde, M.C., "Assessing damage of reinforced concrete beam using “*b*-value” analysis of acoustic emission signals", *Journal of Materials in Civil Engineering ASCE*, **15**:280-6 (2003).
- EN ISO 6892 – 1:2009. Metallic materials -- Tensile testing -- Part 1: Method of test at room temperature (2009).
- Grassberger, P., and Procaccia, I., "Characterization of strange attractors", *Physical Review Letters*, **50**:346-9 (1983).
- Grosse, C., and Ohtsu, M., “Acoustic Emission Testing”, Springer (2008).
- ISIDE Working Group (INGV, 2010), Italian Seismological Instrumental and parametric database: <http://iside.rm.ingv.it>.
- Kapiris, P., Balasis, G., Kopanas, J., Antonopoulos, G., Peratzakis, A., and Eftaxias, K., "Scaling similarities of multiple fracturing of solid materials". *Nonlinear Processes in Geophysics*, **11**:137-51 (2004).
- Katsuyama, K., *In situ application for the use of AE*, Tokyo IPC Press, (1994).
- Kawamoto, S., and Williams, R. S., "Acoustic emission and acousto-ultrasonic techniques for wood and wood-based composites - A review", *Gen. Tech. Rep. FPL-GTR-134*. Madison, WI: U.S. Department of Agriculture, Forest Service, Forest Products Laboratory. (2002).
- Kotsovos, M.D., "Effect of testing technique on the post-ultimate behaviour of concrete in compression", *Materials and Structures*, **16**:3-12 (1983).
- Krajcinovic, D., *Damage Mechanics*, Elsevier, Amsterdam (1996).
- Lagrange, J.-L., *Mécanique Analytique*, Desaint, Paris (1788).
- Landis, E.N., and Shah, S.P., "Frequency-dependent stress wave attenuation in cement-based materials". *J. Eng. Mech.*, **121**:737-43 (1995).

Lemaitre, J., and Chaboche, J.L., *Mechanics of Solid Materials*, Cambridge University Press, Cambridge (1990).

Lockner, D. A., Byerlee, J. D., Kuksenko, V., Ponomarev, A., and Sidorin, A., "Quasi static fault growth and shear fracture energy in granite". *Nature*, **350**:39-42 (1991).

Mogi, K.. "Study of elastic shocks caused by the fracture of heterogeneous materials and its relation to earthquake phenomena". *Bulletin of Earthquake Research Institute*, **40**:125-73 (1962).

Muralidhara, S., Raghu Prasad, B.K., Eskandari, H., and Karihaloo, B.L., "Fracture process zone size and true fracture energy of concrete using acoustic emission". *Constr. Build. Mater.*, **24**:479-86 (2010).

Ohno, K., and Ohtsu, M., "Crack classification in concrete based on Acoustic Emission". *Constr. Build. Mater.*, **24**:2339-46 (2010).

Ohtsu, M., "The history and development of acoustic emission in concrete Engineering", *Magazine of Concrete Research*, **48**:321-30 (1996).

Pollock, A.A., "Stress wave emission - A new tool for industry", *Ultrasonics*, **6**:88-92 (1968).

Pollock, A.A., "Acoustic Emission-2: acoustic emission amplitudes", *Non-Destructive Testing*, **6**:264-69 (1973).

Rao, M.V.M.S., and Lakshmi, K.J.P., "Analysis of b-value and improved b-value of acoustic emissions accompanying rock fracture", *Current Science*, **89**:1577-82 (2005).

Richter, C.F., *Elementary Seismology*, W.H. Freeman, (1958).

RILEM 50-FMC Committee, "Determination of the fracture energy of mortar and concrete by means of three-point bend tests on notched beams", *Materials and Structures*, **18**:286-90 (1986).

- RILEM Technical Committee TC212-ACD: Ohtsu, M., Shiotani, T., Shigeishi, M., Kamada, T., Yuyama, S., Watanabe, T., Suzuki, T., Van Mier, J.G.M., Vogel, T., Grosse, C., Helmerich, R., Forde, M.C., Moczko, A., Breyse, D., Ivanovich, S.A., Sajna, A., Aggelis, D., and Lacidogna, G., "Acoustic Emission and related NDE techniques for crack detection and damage evaluation in concrete: Measurement method for acoustic emission signals in concrete", *Materials and Structures*, **43**:1177-81 (2010a).
- RILEM Technical Committee TC212-ACD: Ohtsu, M., Shiotani, T., Shigeishi, M., Kamada, T., Yuyama, S., Watanabe, T., Suzuki, T., Van Mier, J.G.M., Vogel, T., Grosse, C., Helmerich, R., Forde, M.C., Moczko, A., Breyse, D., Ivanovich, S.A., Sajna, A., Aggelis, D., and Lacidogna, G., "Acoustic Emission and related NDE techniques for crack detection and damage evaluation in concrete: Test method for damage qualification of reinforced concrete beams by Acoustic Emission", *Materials and Structures*, **43**:1183-86 (2010b).
- RILEM Technical Committee TC212-ACD: Ohtsu, M., Shiotani, T., Shigeishi, M., Kamada, T., Yuyama, S., Watanabe, T., Suzuki, T., Van Mier, J.G.M., Vogel, T., Grosse, C., Helmerich, R., Forde, M.C., Moczko, A., Breyse, D., Ivanovich, S.A., Sajna, A., Aggelis, D., and Lacidogna, G., "Acoustic Emission and related NDE techniques for crack detection and damage evaluation in concrete: Test method for classification of active cracks in concrete by Acoustic Emission", *Materials and Structures*, **43**:1187-89 (2010c).
- Rundle, J.B., Turcotte, D.L., Shcherbakov, R., Klein, W., and Sammis, C., "Statistical physics approach to understanding the multiscale dynamics of earthquake fault systems", *Reviews of Geophysics*, **41**:1-30 (2003).
- Scholz, C.H., "The frequency-magnitude relation of microfracturing in rock and its relation to earthquakes", *Bulletin of the Seismological Society of America*, **58**:399-415 (1968).
- Shcherbakov, R., and Turcotte, D.L., "Damage and self-similarity in fracture". *Theoretical and Applied Fracture Mechanics*, **39**:245-58 (2003).
- Soulioti, D., Barkoula, N.M., Paipetis, A., Matikas, T.E., Shiotani T., and Aggelis, D.G., "Acoustic Emission behavior of steel fibre reinforced concrete under bending". *Constr. Build. Mater.*, **23**:3532-6 (2009).

Tinkey, B. V., Fowler, T. J., and Klingner, R. E., "Nondestructive Testing of Prestressed Bridge Girders with Distributed Damage", *Research Report 1857-2, Center for Transportation Research The University of Texas at Austin*, (2002).

Turcotte, D.L., *Fractals and Chaos in Geology and Geophysics*, Cambridge University Press, (1997).

Turcotte, D.L., Newman, W.I., and Shcherbakov, R., "Micro and macroscopic models of rock fracture", *Geophys. J. Int.*, **152**:718-28 (2003).

Van Mier, J.G.M., *Strain softening of concrete under multiaxial compression*, PhD Dissertation, Eindhoven University of Technology, The Netherlands (1984).

Weiss, J., and Marsan, D., "Three-dimensional mapping of dislocation avalanches: clustering and space/time coupling", *Science*, **299**:89-92 (2003).

Zapperi, S., Vespignani, A., and Stanley, H.E., "Plasticity and avalanche behaviour in microfracturing phenomena". *Nature*, **658**:360-388 (1997).